

Department of Physics and Astronomy

University of Heidelberg

Master thesis

in Physics

submitted by

Stefan Lannig

born in Würzburg

2018

Experimental Control of a Spin-1 Bose-Einstein Condensate

This Master thesis has been carried out by Stefan Lannig

at the

Kirchhoff-Institute for Physics

under the supervision of

Prof. Dr. Markus K. Oberthaler

Experimental Control of a Spin-1 Bose-Einstein Condensate

To access the dynamics and internal degrees of freedom in a spin-1 system we present experimental implementation schemes for initial conditions and read-out methods to access the spin projections. For probing non-equilibrium dynamics in spatially extended systems these are essential to identify the underlying processes and relevant degrees of freedom. In our experimental system we employ a quasi-one-dimensional Bose-Einstein condensate of ^{87}Rb in the $F = 1$ hyperfine manifold to tackle these questions. While the only transformations of a spin-1/2 systems are rotations around the three spatial directions, spin-1 particles possess more degrees of freedom. To control their internal state this work provides a set of methods to manipulate both the spinor amplitudes and phases. Furthermore, to access all eight orthogonal spin-1 projections by Stern-Gerlach imaging along a fixed direction different read-out schemes are presented. By applying these techniques spinor phase rotations are implemented which enables controlling of the spin length. This technique is then extended to the spatial domain for generating spin waves. Finally, the read-out methods are applied to measure quadrupole projections in long-time quench dynamics.

Experimentelle Kontrolle eines Spin-1 Bose-Einstein-Kondensates

Um Zugang zur Dynamik und den internen Freiheitsgraden eines Spin-1 Systems zu erhalten, präsentieren wir Strategien zur Implementierung von Anfangszuständen und Auslesemethoden für Spinprojektionen. Diese sind essentiell um bei der Untersuchung von Nichtgleichgewichtsdynamik in räumlich ausgedehnten Systemen die zugrundeliegenden Prozesse und relevanten Freiheitsgrade zu identifizieren. Zur Untersuchung dieser Fragestellungen benutzen wir ein quasi-eindimensionales ^{87}Rb Bose-Einstein-Kondensat in der $F = 1$ Hyperfeinmannigfaltigkeit. Während die einzigen Transformationen eines Spin-1/2-Systems Rotationen um die drei Raumrichtungen sind, besitzen Spin-1-Teilchen eine größere Anzahl an Freiheitsgraden. Zur Kontrolle deren interner Freiheitsgrade zeigt diese Arbeit Methoden, um sowohl die Spinoramplituden als auch -phasen zu manipulieren. Weiterhin werden Ansätze zur Messung aller acht orthogonalen Spin-1-Projektionen durch Absorptionsabbildung mit vorheriger Stern-Gerlach-Separation der magnetsensitiven Zustände entlang einer konstanten Richtung präsentiert. Durch Anwendung dieser Techniken werden Rotationen der Spinorphase implementiert, welche die Kontrolle der Spinlänge ermöglichen. Weiterhin wird diese auf ein räumlich ausgedehntes System angewandt, um Spinwellen zu erzeugen. Zum Abschluss werden Quadrupolprojektionen in der Langzeitdynamik nach einer schnellen Parameteränderung gemessen.

Contents

1	Introduction	1
2	Theoretical Concepts	2
2.1	Spin-1	2
2.1.1	Spin-1 Operators	3
2.1.2	SU(2) Subspaces of Spin-1 Systems	6
2.2	Interactions in ^{87}Rb	7
3	Experimental Setup and Implementation of Spin-1 Techniques	10
3.1	Experimental System and Control	10
3.2	Spin Dipole Rotations	14
3.3	Spin Quadrupole Rotations	17
3.3.1	Readout of Q_{zz} and Rotations around \hat{Q}_{zz}	18
3.3.2	Readout of $\langle \hat{Q}_{xz} \rangle$ and $\langle \hat{Q}_{yz} \rangle$	22
3.3.3	Readout of $\langle \hat{Q}_{xy} \rangle$ and $\langle \hat{Q}_{y^2-x^2} \rangle$	24
4	Measurement of Quadrupole Rotations and Observables	27
4.1	Spinor Phase Evolution of Transversal Spin	27
4.2	Preparation and Control of Spinwaves	37
4.3	Spin Dipole and Quadrupole Observables in Long-Time Dynamics . .	46
4.3.1	Mean-Field Theory	46
4.3.2	Spin-Changing Collision Dynamics	47
4.3.3	Experimental Setup and Read-out of Observables	48
4.3.4	Results	50
5	Conclusion and Outlook	56
A	Additional Plots for Long-Time Dynamics	58
	Bibliography	62

1 Introduction

To study non-equilibrium dynamics [1] in a spatially extended system a high degree of experimental control is required. Identifying the underlying processes necessitates probing their response to the starting point of the dynamics. For this a versatile implementation of initial conditions is required. Similarly important is the realisation of read-out schemes to access the relevant degrees of freedom. While ultracold atoms provide an ideal framework for a precisely controllable system their atomic spin introduces a rich internal structure. [2]

Here, we employ a quasi-one-dimensional Bose-Einstein condensate (BEC) of ^{87}Rb atoms whose $F = 1$ hyperfine manifold provides a spin-1 system. For low temperatures the short-range interactions are incorporated as s -wave scattering. To solve these systems in the limit of large occupation numbers, and correspondingly small fluctuations, often a mean-field approach is applied. This method either neglects the fluctuations or treats them as perturbation. In spin-1 gases these have already been studied extensively [3, 4]. Compared to a spin-1/2 system, here the larger spin provides a higher-dimensional phase space. To manipulate these additional degrees of freedom experimentally, operations must be implemented which go beyond the spin rotations known from spin-1/2 particles. Consequently, transformations of spin-1 particles are described by a larger number of operators, which are associated to the quadrupole moment of the spin-1 particles. [5]

In our setup we apply Stern-Gerlach imaging which projects the spin onto the atomic sublevel densities in quantisation direction. Consequently, to access all spin projections we need to manipulate the system to map the quantities of interest to these densities. Therefore, this work provides schemes to realise the read-out of all eight orthogonal spin-1 operators. Further, techniques for controlling the spin direction and length by adjusting the sublevel densities and phases are presented and applied to implement different initial conditions. In order to provide a comprehensible report, chapter 2 will shortly discuss a theoretical description of the system. Following, chapter 3 summarises the experimental details and techniques for controlling and measuring spin-1 states. These methods are applied in chapter 4 to implement different spin lengths and control spin waves. Finally, an application of the quadrupole read-out after long-time quench dynamics is presented.

2 Theoretical Concepts

This chapter introduces the basic concepts of ultracold spinor gases. We will first consider a general spin-1 system by discussing the properties due to its symmetry. Then, a description of the experimental setup is described, which provides the framework for the control and dynamics of the system that will be discussed afterwards.

2.1 Spin-1

To understand the properties of a spin-1 system, let us start with a short review of the more fundamental spin-1/2 particles. Later, we will see that similar concepts can be applied to the spin-1 case. The wave function of a spin-1/2 object can be specified in the form of a two-component spinor

$$\Psi_{1/2} = e^{i\vartheta} \begin{pmatrix} \sqrt{N_{\uparrow}} e^{i\varphi_L/2} \\ \sqrt{N_{\downarrow}} e^{-i\varphi_L/2} \end{pmatrix}. \quad (2.1)$$

Here, φ_L is the Larmor phase, ϑ an overall phase, and the real amplitudes of both spinor components are constrained by the normalisation $N_{\uparrow} + N_{\downarrow} = 1$. Since in an experiment with only one single object ϑ cannot be measured its value does not influence the state of the system. Thus, as $N_{\downarrow} = 1 - N_{\uparrow}$ is fixed by N_{\uparrow} , a spin-1/2 particle only possesses two free parameters: φ_L and, by choice, N_{\uparrow} . These give rise to a set of allowed transformations which are captured by the Lie group $SU(2)$. It contains the complex unitary 2×2 matrices with unit determinant, which represent length-preserving transformations of complex 2-vectors. Due to this property they can also be considered as rotations of the spinor.

We make the usual choice of the quantisation axis being z . Then, the spin operators are given by $\hat{S}_i = \hat{\sigma}_i/2$ (where we dropped \hbar) with the Pauli matrices

$$\hat{\sigma}_x = \begin{pmatrix} 0 & 1 \\ 1 & 0 \end{pmatrix}, \quad \hat{\sigma}_y = \begin{pmatrix} 0 & -i \\ i & 0 \end{pmatrix}, \quad \text{and} \quad \hat{\sigma}_z = \begin{pmatrix} 1 & 0 \\ 0 & -1 \end{pmatrix}. \quad (2.2)$$

These satisfy the commutation relations of the Lie algebra of $SU(2)$ [6]

$$[\hat{S}_i, \hat{S}_j] = i\epsilon_{ijk}\hat{S}_k, \quad (2.3)$$

where ϵ_{ijk} is the Levi-Civita symbol. Thus, the spin operators \hat{S}_i generate the elements of $SU(2)$. In other words, every possible rotation \hat{U} of a spin-1/2 state can be

written as $\hat{U} = \exp\left(-i \sum_{i=1}^3 r_i \hat{S}_i\right)$ in terms of the spin operators with scalar coefficients r_i . This resembles the form of the time evolution operator for a Hamiltonian composed of spin operators. To understand how this transforms the spin state it is useful to apply the picture of a Bloch sphere, which represents the two-spinors on the surface of a unit sphere. Here, the intersection points of the coordinate axes with the sphere correspond to the eigenstates of the spin operators, i.e. a spin aligned to the corresponding direction. In this picture the evolution operator rotates the state around the axis $\mathbf{r} = (r_1, r_2, r_3)^T$ by the angle $|\mathbf{r}|$. Explicitly, for $\mathbf{r} = (0, \pi/2, 0)$ an \hat{S}_x -eigenstate is rotated to the z -axis. Thus, a time evolution with a spin operator corresponds to a rotation of the spin direction around the corresponding axis.

Extending the spin-1/2 spinor by another component allows the description of a spin-1 system:

$$\Psi_1 = e^{i\vartheta} \begin{pmatrix} \sqrt{N_1} e^{i(\varphi_S/2 + \varphi_L)} \\ \sqrt{N_0} \\ \sqrt{N_{-1}} e^{i(\varphi_S/2 - \varphi_L)} \end{pmatrix}. \quad (2.4)$$

Again, the real amplitudes are constrained by the normalisation $N_1 + N_0 + N_{-1} = 1$ and we will neglect the overall phase ϑ in the following, leaving two amplitudes and two relative phases as free parameters. These additional variables also allow for a larger set of possible rotation directions, which is given by $SU(3)$. Instead of three generators like in the case of $SU(2)$, here there exist eight such operators, which will be introduced in the following section.

Furthermore, by assuming that the wave function of N spins may be written as product state, the normalisation of the spinor (2.4) can be modified to $N = N_1 + N_0 + N_{-1}$, thus allowing the representation of the multi-particle state of these spins. This approximation will be used throughout this work.

2.1.1 Spin-1 Operators

For the experiments discussed in this work a Bose-Einstein condensate of ^{87}Rb is employed. To describe these alkali atoms the choice of spherical harmonics as basis functions is sensible. Thus, in the following we will write its atomic states in terms of the magnetic $m_F = 0, \pm 1$ levels of the $F = 1$ hyperfine manifold as $|F, m_F\rangle$. Since these states provide a spin-1 system we can directly identify the entries of the three-component spinor (2.4) with the magnetic sublevels of the atoms. Instead of representing the complex amplitudes of these basis functions, another approach is specifying the occupation of the corresponding modes in second-quantised form. Here, $\hat{\Psi}_i$ is the annihilation operator for the level i and $\hat{n}_i = \hat{\Psi}_i^\dagger \hat{\Psi}_i$ the corresponding number or density operator. Similar to the spin-1/2 case, also for spin-1 three dipole operators can be derived [7]

$$\hat{F}_i = -i\epsilon_{ijk}\hat{c}_{jk}, \quad (2.5)$$

where we use the Einstein summation convention for $i, j = x, y, z$. Analogous to defining the elements of the operator matrices as $\hat{c}_{ij} = |\phi_i\rangle \langle \phi_j|$, the spin operators can also be described in terms of creation and annihilation operators $\hat{c}_{ij} = \hat{b}_i^\dagger \hat{b}_j$. These Cartesian expressions can be written in the spherical basis as [7]

$$\begin{aligned} |\phi_x\rangle &= \frac{1}{\sqrt{2}} (|1, -1\rangle - |1, 1\rangle) & \hat{b}_x^\dagger &= \frac{1}{\sqrt{2}} (\hat{\Psi}_{-1}^\dagger - \hat{\Psi}_1^\dagger) \\ |\phi_y\rangle &= \frac{i}{\sqrt{2}} (|1, 1\rangle + |1, -1\rangle) & \hat{b}_y^\dagger &= \frac{i}{\sqrt{2}} (\hat{\Psi}_1^\dagger + \hat{\Psi}_{-1}^\dagger) \\ |\phi_z\rangle &= |1, 0\rangle & \hat{b}_z^\dagger &= \hat{\Psi}_0^\dagger \end{aligned} \quad (2.6)$$

To obtain the full set of SU(3) transformations in a spin-1 system, five additional quadrupole operators are required [7]

$$\hat{Q}_{ij} = -\hat{c}_{ij} - \hat{c}_{ji} + \frac{2}{3} \delta_{ij} \hat{c}_{kk}. \quad (2.7)$$

Thus, we obtain eight linearly independent operators which are a full representation of the SU(3) generators:

$$\{ \hat{F}_x, \hat{F}_y, \hat{F}_z, \hat{Q}_{xz}, \hat{Q}_{yz}, \hat{Q}_{xy}, \hat{Q}_{xx}, \hat{Q}_{yy} \}.$$

Additional to these, four more linear combinations $\{ \hat{Q}_{zz}, \hat{Q}_{y^2-x^2}, \hat{Q}_{z^2-y^2}, \hat{Q}_{x^2-z^2} \}$ are of interest. Using the notation $\hat{Q}_{i^2-j^2} := (\hat{Q}_{ii} - \hat{Q}_{jj})/2$, the most frequently used expressions are listed in table 2.1.

Normalisation and Fluctuations

For characterising spin-1 states not only expectation values but also spin dipole fluctuations are of interest. Their size is characterised by standard deviations $\Delta F_i = \sqrt{\langle \hat{F}_i \rangle^2 - \langle \hat{F}_i^2 \rangle}$ of the corresponding operators. A useful quantity to analyse these is the spin covariance matrix [9]

$$T_{ij} = \frac{1}{2} \left\langle [\hat{F}_i, \hat{F}_j]_+ \right\rangle - \langle \hat{F}_i \rangle \langle \hat{F}_j \rangle, \quad (2.8)$$

with $[\cdot, \cdot]_+$ denoting the anticommutator. On the diagonal the matrix contains the variances $\Delta^2 F_i$ of the three dipole operators. Thus, diagonalising the matrix allows extracting the size of the standard deviations and fluctuation directions for any state.

In the experiment the usual number of atoms is $N \sim 10^4$, thus, due to the corresponding spinor normalisation the maximal spin expectation values are also of size N . However, when representing the fluctuations of states this will lead to small standard deviations ΔF_i compared to the maximal size of expectation values $\Delta F_i/N \leq 1/\sqrt{N}$. Thus, when graphically representing the fluctuations for correct

$\hat{F}_x = \frac{1}{\sqrt{2}} \begin{pmatrix} 0 & 1 & 0 \\ 1 & 0 & 1 \\ 0 & 1 & 0 \end{pmatrix}$	$\hat{F}_x = \frac{1}{\sqrt{2}} \hat{\Psi}_0^\dagger (\hat{\Psi}_1 + \hat{\Psi}_{-1}) + h.c.$
$\hat{F}_y = \frac{i}{\sqrt{2}} \begin{pmatrix} 0 & -1 & 0 \\ 1 & 0 & -1 \\ 0 & 1 & 0 \end{pmatrix}$	$\hat{F}_y = \frac{i}{\sqrt{2}} \hat{\Psi}_0^\dagger (\hat{\Psi}_1 - \hat{\Psi}_{-1}) + h.c.$
$\hat{F}_z = \begin{pmatrix} 1 & 0 & 0 \\ 0 & 0 & 0 \\ 0 & 0 & -1 \end{pmatrix}$	$\hat{F}_z = \hat{n}_1 - \hat{n}_{-1}$
$\hat{Q}_{xz} = \frac{1}{\sqrt{2}} \begin{pmatrix} 0 & 1 & 0 \\ 1 & 0 & -1 \\ 0 & -1 & 0 \end{pmatrix}$	$\hat{Q}_{xz} = \frac{1}{\sqrt{2}} \hat{\Psi}_0^\dagger (\hat{\Psi}_1 - \hat{\Psi}_{-1}) + h.c.$
$\hat{Q}_{yz} = \frac{i}{\sqrt{2}} \begin{pmatrix} 0 & -1 & 0 \\ 1 & 0 & 1 \\ 0 & -1 & 0 \end{pmatrix}$	$\hat{Q}_{yz} = \frac{i}{\sqrt{2}} \hat{\Psi}_0^\dagger (\hat{\Psi}_1 + \hat{\Psi}_{-1}) + h.c.$
$\hat{Q}_{xy} = \begin{pmatrix} 0 & 0 & -i \\ 0 & 0 & 0 \\ i & 0 & 0 \end{pmatrix}$	$\hat{Q}_{xy} = i \hat{\Psi}_{-1}^\dagger \hat{\Psi}_1 + h.c.$
$\hat{Q}_{xx} = \begin{pmatrix} -\frac{1}{3} & 0 & 1 \\ 0 & \frac{2}{3} & 0 \\ 1 & 0 & -\frac{1}{3} \end{pmatrix}$	$\hat{Q}_{xx} = \frac{1}{3} (2\hat{n}_0 - \hat{n}_1 - \hat{n}_{-1}) + \hat{\Psi}_1^\dagger \hat{\Psi}_{-1} + \hat{\Psi}_{-1}^\dagger \hat{\Psi}_1$
$\hat{Q}_{yy} = \begin{pmatrix} -\frac{1}{3} & 0 & -1 \\ 0 & \frac{2}{3} & 0 \\ -1 & 0 & -\frac{1}{3} \end{pmatrix}$	$\hat{Q}_{yy} = \frac{1}{3} (2\hat{n}_0 - \hat{n}_1 - \hat{n}_{-1}) - \hat{\Psi}_1^\dagger \hat{\Psi}_{-1} - \hat{\Psi}_{-1}^\dagger \hat{\Psi}_1$
$\hat{Q}_{zz} = \begin{pmatrix} \frac{2}{3} & 0 & 0 \\ 0 & -\frac{4}{3} & 0 \\ 0 & 0 & \frac{2}{3} \end{pmatrix}$	$\hat{Q}_{zz} = \frac{2}{3} (\hat{n}_1 + \hat{n}_{-1} - 2\hat{n}_0)$
$\hat{Q}_{y^2-x^2} = \begin{pmatrix} 0 & 0 & -1 \\ 0 & 0 & 0 \\ -1 & 0 & 0 \end{pmatrix}$	$\hat{Q}_{y^2-x^2} = -\hat{\Psi}_1^\dagger \hat{\Psi}_{-1} + h.c.$

Table 2.1: Spin-1 operators in the basis $|F = 1, m_F\rangle$. The first eight operators are a representation of the linearly independent generators of SU(3). [8]

experimental values their extent would not be visible. To avoid this, for graphs showing the size of this quantity a much smaller value of N will be used.

Majorana Representation

A further useful insight into the properties of spin-1 systems is their representation as two spin-1/2 particles. [2, 4] This way, the system can be pictured as two vectors on a Bloch sphere. When these spins are pointing into the same direction their vector addition results in a fully elongated spin-1 state along the corresponding direction. Rotating one spin-1/2 direction while keeping the other constant results in a reduced length of the vectorial sum which reaches zero for antiparallel alignment. This resembles the reduction of the spin projection in the corresponding direction until it reaches zero in all projections. Further, by considering the dipole fluctuations of the single spin-1/2 states these can also be transferred to spin-1. The single 1/2-components always exhibit fluctuations perpendicular to the direction in which their spin vector is pointing. Consequently, for a fully extended spin-1 state composed of two spin-1/2 vectors oriented along the same axis the fluctuations are also confined to the perpendicular plane. In case of antiparallel spin-1/2 alignment this is equally valid. However, in contrast to the fully extended spin projection in some direction, here only the plane containing the fluctuations specifies a direction of the state. When aligned to the appropriate axes, the former spin-1 states are eigenstates of the dipole operators while the latter are eigenstates of the quadrupoles. To contrast these quadrupole from the usual dipole components these states are also called polar, nematic, or aligned. [10]

2.1.2 SU(2) Subspaces of Spin-1 Systems

As we have seen in the example of spin-1/2 particles, the action of the three spin operators can be understood as rotations of the spin state around the Bloch sphere axis corresponding to the respective operator. In spin-1 systems, however, matters are more complex in the sense that there are more rotation axes and, due to the additional degrees of freedom, a spin-1 state cannot be represented by a single point on the surface of a Bloch sphere. Nevertheless, the symmetry of spin-1 particles allows their generators of rotations, i.e. the dipole and quadrupole operators introduced in the previous section, to be divided into triples $\{\hat{O}_1, \hat{O}_2, \hat{O}_3\}$. Each of these satisfies the spin-1/2 commutation relations $[\hat{O}_i, \hat{O}_j] = i\epsilon_{ijk}\hat{O}_k$. For the spin-1 system the following triples may be found [7]

$$\begin{array}{ll}
 \{ \hat{F}_x, \hat{F}_y, \hat{F}_z \} & \{ \hat{F}_x, \hat{Q}_{yz}, \hat{Q}_{z^2-y^2} \} \\
 \{ \hat{Q}_{xz}, \hat{Q}_{yz}, \hat{F}_z \} & \{ \hat{F}_y, \hat{Q}_{xz}, \hat{Q}_{x^2-z^2} \} \\
 \{ \hat{F}_x, \hat{Q}_{xz}, \hat{Q}_{xy} \} & \{ \hat{F}_z, \hat{Q}_{xy}, \hat{Q}_{y^2-x^2} \} \\
 \{ \hat{F}_y, \hat{Q}_{yz}, \hat{Q}_{xy} \} &
 \end{array}$$

Here, to obtain the commutator relations for the sets in the right column one has to multiply each of the operators with a factor $-1/2$. As consequence each of these subsets have the same properties as the spin-1/2 operators. To illustrate this, let us exemplarily consider a rotation in the third subgroup with the initial state being an eigenstate of \hat{Q}_{xz} . Then, analogous to the Bloch-sphere picture for spin-1/2 rotations, the time evolution with a Hamiltonian composed of \hat{Q}_{xy} will rotate the state around the Q_{xy} -axis. This eventually transforms the initial \hat{Q}_{xz} eigenstate to a \hat{F}_x eigenstate. Thus, by applying these divisions to the spin-1 space allows understanding the action of spin-1 operators as rotations in the corresponding subspaces. In chapter 3 we will illustrate this further.

2.2 Interactions in ^{87}Rb

In cold dilute gases with small atomic spin the interactions between ground state atoms can predominantly be described by contact interactions. For a Rubidium condensate the low-energy s -wave scattering allows a good approximation of these, which means that in atomic collisions the total spin of the particles is conserved. [11] The resulting second-quantised Hamiltonian $\hat{\mathcal{H}}$ [4] of the $F = 1$ hyperfine manifold of bosonic ^{87}Rb in a trapping potential can be divided into three parts:

$$\hat{\mathcal{H}} = \int d^3r \left(\hat{\mathcal{H}}_0 + \hat{\mathcal{H}}_B + \hat{\mathcal{H}}_{\text{int}} \right). \quad (2.9)$$

The single-particle term

$$\hat{\mathcal{H}}_0 = \sum_i \hat{\Psi}_i^\dagger(\mathbf{r}) \left(\frac{\hbar^2 \nabla^2}{2m} + V_{\text{trap}}(\mathbf{r}) \right) \hat{\Psi}_i(\mathbf{r}) \quad (2.10)$$

contains the kinetic energy and the potential V_{trap} confining the atoms. Because the experiments are carried out in an external magnetic field the resulting shifts must be taken into account. Capturing these,

$$\hat{\mathcal{H}}_B = \hbar p \hat{F}_z(\mathbf{r}) + \hbar q (\hat{n}_1(\mathbf{r}) + \hat{n}_{-1}(\mathbf{r})) \quad (2.11)$$

contains the linear and second-order Zeeman frequency shifts p and q , respectively (they are discussed more extensively in section 3.1). Finally, to describe the inter-particle scattering processes the bosonic exchange symmetry must be taken into account. Therefore, two particle pair spin channels $\mathcal{F} = 0, 2$ are relevant for spin-1 particles. Combined, these are described by

$$\hat{\mathcal{H}}_{\text{int}} =: (c_0 \hat{n}^2(\mathbf{r}) + c_1 (\hat{F}_x^2(\mathbf{r}) + \hat{F}_y^2(\mathbf{r}) + \hat{F}_z^2(\mathbf{r}))) :, \quad (2.12)$$

where $:\cdot:$ denotes normal-ordering, $\hat{n} = \sum_i \hat{n}_i$ is the total density operator, and

$$c_0 = \frac{4\pi\hbar^2}{m} \frac{a_0 + 2a_2}{3}, \quad \text{and} \quad (2.13)$$

$$c_1 = \frac{4\pi\hbar^2}{m} \frac{a_2 - a_0}{3}$$

are the density-density and spin-spin coupling constants, respectively, with m being the atomic mass of Rubidium. Values for the s -wave scattering lengths $a_{\mathcal{F}}$ for the relevant boson pair spin channels $\mathcal{F} = 0, 2$ can be found in [2]. Because in this work we are interested in spin physics we assume the atoms to initially be motional ground state and do not induce density excitations. Consequently, the net density remains in a stationary state and we can drop the terms which only depend on \hat{n} . This also includes $\hat{\mathcal{H}}_0$ because in the momentum space this can be reformulated in terms of the total density \hat{n} . Note also that due to the conservation of spin in the s -wave scattering the F_z projection of the spin stays constant. Consequently, the linear Zeeman shift does not influence the collisional spin dynamics. Thus, the external-field dependent term setting the energy scale for the inter-particle dynamics is the second-order Zeeman shift.

System Dimensionality and Single-Mode Approximation

The harmonic trap used in the experiment confines the atoms in transversal direction to the lowest harmonic oscillator levels. Due to the anisotropy of the trap, however, longitudinally the atoms occupy a much larger range of oscillator states. Thus, for the following arguments we will assume a one-dimensional system along the x -axis. To capture this spatial dependence, the field operators can be expanded in terms of annihilation operators \hat{a}_{mi} of a particle in the magnetic state m and spatial mode i , and the corresponding basis functions $\phi_{mi}(x)$ [4]

$$\hat{\Psi}_m(x) = \sum_i \hat{a}_{mi} \phi_{mi}(x). \quad (2.14)$$

For three-dimensional systems that are much smaller than the spin-healing length $\xi_s = \hbar/\sqrt{2m|c_1|n}$ in all directions, the single-mode approximation can be applied. [12, 8] This approach fixes the sum in eq. (2.14) to one contribution in i and allows to neglect the spatial dependence of the dynamics. Here, however, this approximation cannot be applied for the longitudinal direction. Nevertheless, when driving the system on timescales shorter than the one of spin dynamics, we may neglect the interaction effects and consider the system to be homogeneous. However, to estimate the interaction time scales we have to take the dimensionality of the system into account. This modifies the coupling constants such that $c_1^{(1D)} = 2\hbar(a_2 - a_0)/(3ma_{\perp})$ [13] with the transversal harmonic oscillator length $a_{\perp} = \sqrt{\hbar/(m\omega_{\perp})}$ in a trap with corresponding angular oscillator frequency ω_{\perp} . To estimate the energy scale associated to the spin-spin interactions we assume a mean field shift $c_1^{(1D)}n^{(1D)}$ resulting from a generic mean-field treatment. Inserting the usual trap frequency (see section 3.1) and peak density $n^{1D} \approx 350 \mu\text{m}^{-1}$ leads to a dynamical time scale of ~ 200 ms. Thus, for all processes that are much faster than this the system can be assumed to be homogeneous. Since the time evolutions considered in chapter 3 are shorter than 10 ms this condition is well satisfied.

Bogoliubov Approximation and Mean-Field Dynamics

To further analyse the collisional dynamics we expand the spin-dependent part of $\hat{\mathcal{H}}_{\text{int}}$ (with $\hat{\mathbf{F}}^2 = \hat{F}_x^2 + \hat{F}_y^2 + \hat{F}_z^2$ as short-hand notation of the spin-spin interaction term)

$$\begin{aligned} : \hat{\mathbf{F}}^2 : &= 2 \left(\hat{\Psi}_0^\dagger \hat{\Psi}_0^\dagger \hat{\Psi}_1 \hat{\Psi}_{-1} + \hat{\Psi}_1^\dagger \hat{\Psi}_{-1}^\dagger \hat{\Psi}_0 \hat{\Psi}_0 \right) + 2 (\hat{n}_0 (\hat{n}_1 + \hat{n}_{-1}) - \hat{n}_1 \hat{n}_{-1}) \\ &+ : \hat{n}_1^2 + \hat{n}_{-1}^2 : \end{aligned} \quad (2.15)$$

Here, the first two terms describe spin-changing collisions (SCCs) which redistribute atoms between the hyperfine levels and the remaining terms introduce energy shifts of the corresponding levels. By applying the Bogoliubov approximation $\hat{\Psi}_i = \Psi_i + \delta \hat{\Psi}_i$, which assumes operators to be complex fields with only a small non-commuting contribution, the Hamiltonian can be evaluated in the mean-field framework. [13] Thus, neglecting the fluctuations, the operators can be replaced by their expectation values. Note however, that this treatment is only applicable if the population of the corresponding m_F levels is large such that the fluctuations are small.

3 Experimental Setup and Implementation of Spin-1 Techniques

3.1 Experimental System and Control

After discussing the structure of spin-1 systems and a short overview over the mechanisms driving dynamics in atomic gases of ^{87}Rb we now turn to the experimental system and accessing the spin-1 degrees of freedom. The platform employed in this work consists of a quasi-one-dimensional BEC of ^{87}Rb atoms whose $F = 1$ hyperfine manifold provides the spin-1 system studied here. First, this chapter will give a short overview of the experimental system before providing schemes for implementing the readout of different spin-observables and various rotations in the spin space.

Overview

Each experimental cycle starts with collecting atoms in a three-dimensional magneto-optical trap (MOT) by loading from a two-dimensional MOT. Afterwards, the atomic cloud is compressed, followed by polarisation gradient cooling and evaporation in a time-orbiting magnetic potential. [14] Finally, a 1030 nm laser, far red-detuned to the D_1 and D_2 transitions of ^{87}Rb , is switched on, which induces dipole forces that provide a trapping potential. For the process of transferring the atoms from the magnetic trap two such beams are crossed and the magnetic fields are ramped down. Next, by decreasing the laser power another step of evaporative cooling lowers the temperature of the cloud below the critical temperature of the Bose-Einstein condensation transition. Afterwards, one of the laser beams is ramped down and the atoms expand in the optical potential of the remaining beam. This waveguide confinement is approximately harmonic with frequencies $\omega_{\perp} \approx 2\pi \times 250$ Hz in the radial and $\omega_x \approx 2\pi \times 2.2$ Hz in the longitudinal direction. The resulting cloud of condensed atoms has a size of about 250 μm longitudinally and 1 μm transversally (see fig. 3.1). Alternatively, the second beam can be kept at full power to confine the atoms in a crossed dipole trap which effectively increases the longitudinal frequency to $\omega_x \approx 2\pi \times 50$ Hz.

Thus, the trapping and cooling cycle described above, which lasts for about 37 s, produces a BEC of $\sim 70\,000$ ^{87}Rb atoms in the $|F = 1, m_F = -1\rangle$ hyperfine state of their $5^2\text{S}_{1/2}$ ground state. This is the starting point for all experiments performed throughout this work.

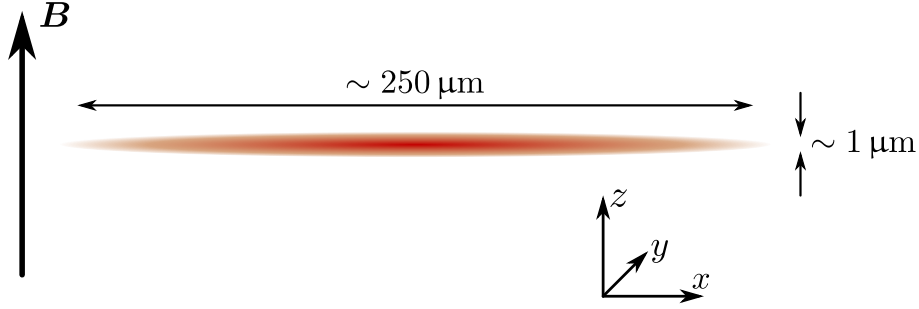


Figure 3.1: Schematic overview of the waveguide trap geometry.

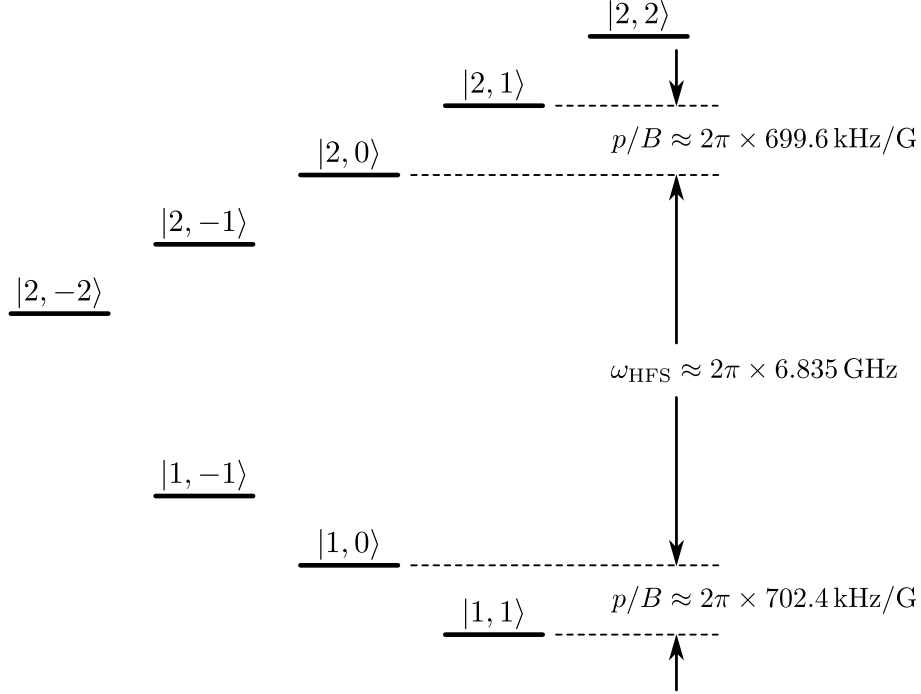
Level Structure of the ^{87}Rb Groundstate [15]

In small magnetic fields the coupling between the nuclear spin $I = 3/2$ of this Rubidium isotope and its single $5s$ valence electron with spin $S = 1/2$ give rise to two hyperfine manifolds $F = 1, 2$. These are separated by $\omega_{\text{HFS}} \approx 2\pi \times 6.835$ GHz and their magnetic sublevels exhibit a linear Zeeman splitting of $p = \mu_B g_F m_F B$ in magnetic bias fields $B = |\mathbf{B}|$. Here, μ_B is the Bohr magneton and $g_{F=1} = -1/2$ and $g_{F=2} = 1/2$ are the Landé g -factors for the $F = 1$ and $F = 2$ levels, respectively. Resulting from this splitting a Larmor precession of the spin direction in the plane orthogonal to \mathbf{B} at angular frequency p arises. The experimentally accessible states and their energetic shifts is schematically shown in fig. 3.2a). Additionally to the linear Zeeman shift, expanding the Breit-Rabi formula to quadratic contributions in the magnetic field $q = (g_J - g_I)^2 \mu_B^2 / (16\hbar^2 \omega_{\text{HFS}}) B^2$ gives rise to the much smaller second-order Zeeman shift. A transformation to the co-rotating Larmor frame removes the linear shift and reveals the detuning of the side modes $m_F = \pm 1$ compared to the zero mode $m_F = 0$. This second-order Zeeman splitting (see fig. 3.2b) controls the energetic detuning of the collisional spin dynamics.

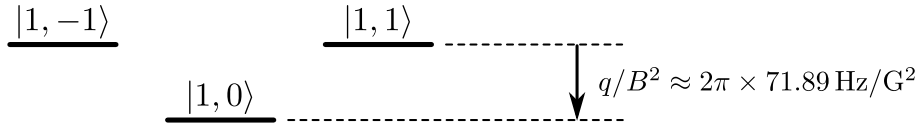
Experimental Control: MW and RF Pulses

Engineering initial states or selecting various spin observables requires coupling the different hyperfine levels. Experimentally, this is achieved by applying oscillating magnetic fields in the microwave (MW) or radio frequency (RF) regime at frequencies of about 6.8 GHz or 600 kHz, respectively. Because the Rabi frequencies associated with these couplings are much larger than the frequency splittings relevant for spin dynamics the collisional spin interactions can be neglected here. On the apparatus there exist two types of antennas for generating the required fields: a single copper loop for MW fields and coils for RF signals.

First, let us focus on how MW signals affect the internal states of the atoms. Due to the geometry of the antenna the MW fields consist of a superposition of all polarisations, albeit not with equal intensity. By operating the experiment at constant bias fields in the range $B \approx 0.9$ G, the application of MW fields allows selective pairwise coupling between one of the $F = 1$ and one of the $F = 2$ states.



(a) Splitting of $F = 1$ and $F = 2$ manifolds in an external magnetic field.



(b) Second-order Zeeman shift of the $F = 1$ states in the co-rotating Larmor frame.

Figure 3.2: **a)** Schematic display of the $F = 1, 2$ linear Zeeman splitting in ^{87}Rb using the notation $|F, m_F\rangle$. Due to small deviations of the electronic and nuclear g -factors from $g_J = 2$ and $g_I = 0$ there is a small difference in the $F = 1$ and $F = 2$ splitting. **b)** Level scheme in the rotating Larmor frame with second-order Zeeman shift q .

Tuning the MW frequency to resonance with a certain transition the other levels experience a far off-resonant coupling with a detuning of ca. 0.6 MHz induced by the linear Zeeman shift. Thus, the transfer amplitudes for these other couplings are negligible. Nevertheless, transitions which are degenerate with respect to the linear Zeeman shift (e.g. $|1, -1\rangle \leftrightarrow |2, 0\rangle$ and $|1, 0\rangle \leftrightarrow |2, -1\rangle$) this argument does not hold and the second transition is only detuned by a frequency proportional to the second-order Zeeman shift. Here, care must be taken that the other coupling does not disturb the desired effect of the MW pulse.

In contrast to MW coupling, RF fields drive transitions between the magnetic sublevels within a hyperfine manifold. Section 3.2 will discuss this type of coupling in detail.

Imaging the Atoms [16]

In each cycle after the evolution period an imaging sequence extracts the atomic densities in the three magnetic sublevels with spatial resolution along the longitudinal direction. Following the experimental period with a delay of a few ms a strong quadrupole field is applied for the duration of 3 ms. This results in a Stern-Gerlach separation of the sublevels in the magnetic gradient field along the quantisation axis. During the pulse the confining dipole trap is switched off such that after the pulse the atoms expand freely for 1 ms. This leads to a spatial separation of the different magnetic sublevels. Directly following this time-of-flight period the cloud is imaged by high-intensity absorption imaging. To distinguish the two hyperfine manifolds two measurements are taken which extract the atomic absorption during illumination with 15 μ s long imaging pulses. The first one consists of D_2 light resonant to the $F = 2 \rightarrow F' = 3$ transition which measures and removes the $F = 2$ atoms. Then, after about 1 ms another pulse mixes the previous imaging light with re-pumper light resonant to $F = 1 \rightarrow F' = 2$ to address the $F = 1$ manifold. Finally, two reference pictures are taken to infer the exact size of the absorption and remove the camera offset. Consequently, by inference from the absorption this technique extracts the local atom numbers pixel for each magnetic sublevel separately.

Conclusions

Summarising the experimental capabilities of this ultracold atom system, the spin state of the particles can be precisely controlled. Further, Stern-Gerlach imaging allows accessing the magnetic sublevel densities $\langle \hat{n}_i \rangle$ by projection along the quantisation axis. Coherences $\langle \hat{\Psi}_i^\dagger \hat{\Psi}_j \rangle$ for $j \neq i$, on the other hand, which appear in many spin operators like \hat{F}_x , \hat{F}_y , or \hat{Q}_{xy} cannot be accessed directly. Nevertheless, applying rotations around different axes of the spin space enables the access to a larger set of observables by mapping the quantity of interest to densities in the three magnetic sublevels. Implementing these rotations and mappings for a number of spin operators for the $F = 1$ system will be addressed in the following.

3.2 Spin Dipole Rotations

Transferring the method from the manipulation of spin-1/2 systems, rotations around the three spin axes F_x , F_y , and F_z are possible in the SU(3) spin space in an equivalent manner. As described in chapter 2 the corresponding spin dipole operators \hat{F}_i are the generators of rotations in this space of expectation values F_i .

To enable these operations experimentally, the three magnetic sublevels are coupled with each other via oscillating RF fields. These oscillate in a plane perpendicular to the magnetic bias field which is oriented orthogonal to the longitudinal direction of the cloud (x - y -plane in fig. 3.1) at a frequency matching p . The resulting Hamiltonian in the rotating Larmor frame can be derived by considering two independent two-level systems with identical resonant Rabi frequencies Ω_{RF} . While the RF-frequency can be adjusted very well to match the linear Zeeman shift, an important type of residual detuning is the energetic shift of the side modes $m_F = \pm 1$ by δ such that $m_F = 0$ is not centred in the $F = 1$ manifold any more. In the $|1, 0\rangle \leftrightarrow |1, -1\rangle$ system this introduces the detuning $+\delta$ while in the other one ($|1, 1\rangle \leftrightarrow |1, 0\rangle$) the detuning from resonance is $-\delta$. Writing both contributions as a matrix in the usual basis yields

$$\begin{aligned}\hat{\mathcal{H}}_{\text{RF}}(\varphi) &= \frac{\hbar}{\sqrt{2}} \begin{pmatrix} -\delta & e^{-i\varphi}\Omega_{\text{RF}} & 0 \\ e^{i\varphi}\Omega_{\text{RF}} & 2\delta & e^{-i\varphi}\Omega_{\text{RF}} \\ 0 & e^{i\varphi}\Omega_{\text{RF}} & -\delta \end{pmatrix} \\ &= \hbar\Omega_{\text{RF}} \left(\cos(\varphi)\hat{F}_x - \sin(\varphi)\hat{F}_y \right) + \frac{3}{2\sqrt{2}}\hbar\delta\hat{Q}_{zz},\end{aligned}\tag{3.1}$$

where φ denotes the phase of the RF signal. Usually, the detuning for the coupling pulses is predominantly given by the second-order Zeeman shift $\delta = q$. Thus, for short pulses with usual experimental Rabi frequency $\Omega_{\text{RF}} = 2\pi \times 17$ kHz the \hat{Q}_{zz} term introduced by the detuning can be dropped.

As we have seen in section 2.1.2 the three spin dipole operators $\{\hat{F}_x, \hat{F}_y, \hat{F}_z\}$ form a SU(2) subspace, which means a spin-1 particle whose evolution is described by a Hamiltonian involving only the dipole operators behaves like a spin-1/2 system. Thus, analogous to such a system, the time evolution of a spin-1 state under one of these operators rotates the wave function within the corresponding subset of states with constant spin length. However, to understand the physical meaning of these rotations we want to observe their action on the spin expectation value $\mathbf{F} = \langle \Psi | \hat{\mathbf{F}} | \Psi \rangle$ with $\hat{\mathbf{F}} := (\hat{F}_x, \hat{F}_y, \hat{F}_z)^T$ rather than the transformation of the corresponding spinor $|\Psi\rangle$. To reduce the notational complexity, in the following only rotations around F_y will be considered, although it should be noted that this argument can be generalised to any axis. Evolving an arbitrary state $|\Psi\rangle$ under the Hamiltonian $\hat{\mathcal{H}} = \Omega_{\text{RF}}\hat{F}_y$ for a time $t = \theta/\Omega_{\text{RF}}$ rotates the spin expectation vector in the following way (see fig. 3.3a):

$$e^{-i\theta\hat{F}_y} |\Psi\rangle \mapsto \mathcal{R}_y(\theta)\mathbf{F}.\tag{3.2}$$

Here $\mathcal{R}_y(\theta)$ resembles the transformation matrix for a rotation around the y -axis by an angle θ in real 3-dimensional space. As such the transformations generated by the spin dipole operators have the property to conserve the spin length while allowing an arbitrary change in the spin direction.

Graphical Representation of a Spin-1 System

Similar to the visualisation of a spin-1/2 spinor on the surface of the Bloch sphere the spin-1 vector \mathbf{F} , because its length is limited to a maximum of the particle number, can also be represented inside such a sphere. However, there exists a crucial difference: in the former case the full spin-1/2 wave function is represented while the latter only fixes three expectations values of the state. For spin-1/2 the polar and azimuthal angle suffice to fully specify all degrees of freedom of the system. In contrast, a spin-1 particle possesses more than three free parameters such that it is not uniquely defined by the components of \mathbf{F} . Furthermore, unlike the Bloch sphere picture that only utilises the surface, for spin-1 \mathbf{F} can also access the entire volume of the sphere. Thus, to clarify the difference between a Bloch sphere representation and plotting the spin expectation value, let us use the term “spin sphere” whenever referring to a representation of spin expectation values. To allow a more explicit visualisation of the spin states additional to \mathbf{F} also the dipole fluctuations of the state are shown. These are calculated by diagonalising the spin covariance matrix (2.8) for the corresponding spin-1 state. The spatial extent of the standard deviations are shown by an ellipsoid whose half axes are given by the eigenvectors scaled by the corresponding eigenvalues.

The picture introduced above allows the interpretation of complex dynamical effects which can be formulated in terms of spin dipole operators as rotations in the spin sphere. Figure 3.3 illustrates the behaviour of a spin-1 system under evolution with different operators. In the experiment a specific transversal rotation axis can be chosen by setting the phase φ accordingly (see eq. (3.1)). Thus, the RF-rotations allow well-controlled rotations in the spin sphere.

Experimental Application of Spin Dipole Rotations

As we have seen, spin-1 states can be rotated around the F_i axes arbitrarily, such that initial states of any spin direction may be prepared. x - and y -rotations can be implemented via RF coupling while z -rotations can be achieved by Larmor precession in the external magnetic field. Then, after evolving the system with a specific Hamiltonian the quantity of interest needs to be extracted. Section 3.1 described that the only experimentally accessible observables in the system are the atomic densities n_i of the magnetic sublevels. This allows the direct measurement of F_z , however, to access the coherences contained in the other spin projections the state needs to be rotated first. Here, the same techniques which allow the generation of arbitrary spin directions in initial states also enable the access to these projections as observables. Prior to the imaging sequence, the preferred spin axis can be rotated

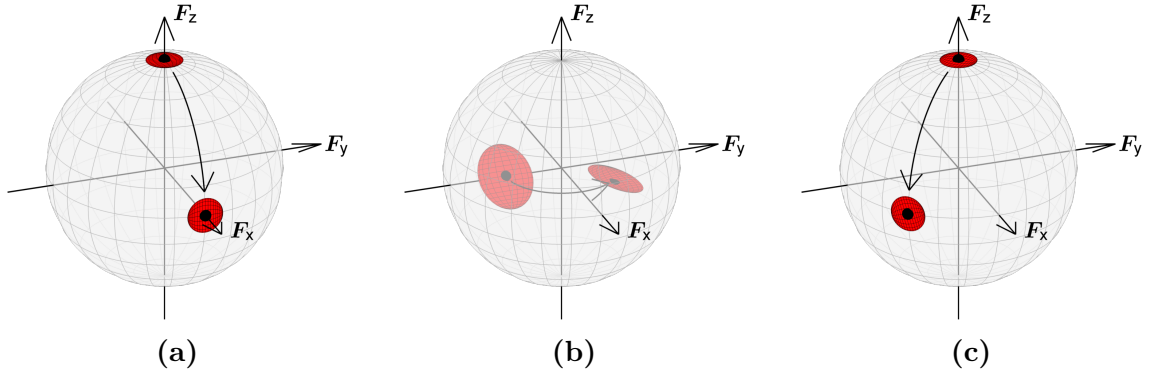


Figure 3.3: Visualisation of different rotations in the spin sphere of expectation values. For the states discussed here the dipole expectation value \mathbf{F} is marked with a black dot. Additionally, the red ellipsoid shows the directions and amplitudes of the corresponding fluctuations for an atom number of $N = 10$. Its half axes are calculated from the eigenvectors and eigenvalues of the spin covariance matrix (2.8). **a)** $\theta = \pi/2$ rotation of an aligned z -spin to the transversal plane by a rotation with \hat{F}_y . **b)** Time evolution of the state $|\Psi\rangle = 1/2(1, 1 - i, -i)^T$ with \hat{F}_z (Larmor rotation around external magnetic field) in the transversal plane by $\theta = 3\pi/4$. The state has spin length $|\mathbf{F}| = 0.5$ which is preserved throughout the transformation. In rough approximation the initial fluctuation ellipsoid resembles a disk tilted around the y -axis which rotates along with the RF-rotation. **c)** $\theta = \pi/2$ evolution with $\hat{\mathcal{H}}_{\text{RF}}$ (eq. (3.1)) for $\varphi = \pi/4$.

to the z -direction, allowing its readout via sublevel densities. Note however, that due to fluctuations in the external magnetic field the error on the absolute angle of the read-out direction in the x - y -plane grows with time. Thus, after long times a projection axis cannot be imaged with a reproducible relative angle to the initial state preparation direction. Instead, for multiple fast pulses in short succession their relative phases can be controlled with high stability.

Mathematically, the read-out of a rotated projection direction can be represented as time-evolving the state $|\Psi\rangle$ of interest with the operators required to generate the desired rotations. Let us exemplarily consider the readout of a spin aligned to the x -axis. Corresponding to the operation displayed in fig. 3.3a, the desired read-out mapping is implemented by a $\theta = -\pi/2$ rotation with \hat{F}_y . Thus, writing down the expectation value extracted in z -direction by the imaging subsequent to the rotation scheme results in

$$\langle\Psi|e^{-i\frac{\pi}{2}\hat{F}_y}\hat{F}_ze^{i\frac{\pi}{2}\hat{F}_y}|\Psi\rangle = \langle\Psi|\hat{F}_x|\Psi\rangle \quad (3.3)$$

shows that the observable extracted by this readout scheme indeed is \hat{F}_x . As before, this technique can be generalised to read out any direction by extracting the correct order of operator application and corresponding angles by consideration of the rotations in the spin sphere.

Concluding, we have seen that in a time-evolution the action of spin-1 dipole operators, which build a $SU(2)$ subspace, are rotations of the spin direction while preserving the length. To visualise these transformations, the spin sphere was introduced, which allows the full representation of all associated $SU(2)$ transformations. Implementing these operators via RF-pulses thus allows the preparation of initial states with arbitrary spin directions. Further, these techniques can be applied to map any spin direction to the quantisation axis z . The corresponding spin observable \hat{F}_z is directly accessible via Stern-Gerlach absorption imaging.

3.3 Spin Quadrupole Rotations

In the previous section we investigated the dipole operators, which are routinely applied in experiments on spin-1/2 systems. However, as discussed in section 2.1 a spin-1 particle possesses additional degrees of freedom which are associated with the spin quadrupole operators \hat{Q}_{ij} . Thus, they are of similar importance as the spin dipoles for the control and read-out of spin-1 systems. Generally, accessing these operators requires a different approach than the one presented for the transversal spin projections. Since the quadrupoles contain coherences between different sub-levels these are probed by coupling them among each other. Here, multiple RF- and MW-pulses as well as time evolutions in the external magnetic field are required for the read-out.

A useful insight into the spin system is the realisation that the $SU(3)$ subdivision into $SU(2)$ groups discussed in section 2.1.2 allows the treatment of a small set of observables analogous to a spin-1/2 system. Thus, to read out certain quadrupoles,

first a rotation in a subspace containing the operator of interest is performed which maps the observable to a dipole direction. Utilising the RF techniques described in the previous section, this dipole, in turn, can be mapped to the quantisation axis for imaging. Consequently, most quadrupole operators can be extracted via this two-step scheme. At first, however we want to consider direct implementations of quadrupole operators before turning to the manipulation of complete subspaces.

3.3.1 Readout of Q_{zz} and Rotations around \hat{Q}_{zz}

The only quadrupole operator not containing two-level coherences is

$$\hat{Q}_{zz} = \begin{pmatrix} \frac{2}{3} & 0 & 0 \\ 0 & -\frac{4}{3} & 0 \\ 0 & 0 & \frac{2}{3} \end{pmatrix}. \quad (3.4)$$

Thus, this observable can be measured in the z -basis by extracting the densities via Stern-Gerlach imaging without the requirement for prior rotations.

On the other hand, implementing rotations with this operator requires a new approach. Considering the form of the coupling matrix (3.4) the action of this operator results in an energy shift of the sublevels without driving population transfers. In general, as long as the coupling period is sufficiently short any collisional spin-spin dynamics can be neglected. Thus, at large external fields the second-order Zeeman shift, which generates an additional phase evolution of the side modes $m_F = \pm 1$, can be utilised to implement this operator. Here, MW dressing can reduce the time required to implement these coupling pulses by energetically shifting the zero mode $m_F = 0$.

First, we want to consider the energetic shift of the levels in an external magnetic field \mathbf{B} . By transforming to a frame co-rotating with the Larmor precession, the linear Zeeman shift generated by the \mathbf{B} -field can be dropped in the effective Hamiltonian of the system. To understand this, we apply an approach analogous to the transformation used for obtaining interaction picture operators [17]. Here, the idea is to remove the action of a solvable part of the Hamiltonian to focus on the more complex, “interacting” part. Consequently, $\hat{\mathcal{H}}_B$ from eq. (2.11) is divided into the linear and second-order Zeeman contributions $\hat{\mathcal{H}}_{B,0} = \hbar p \hat{F}_z$ and $\hat{\mathcal{H}}'_B = \hbar q \hat{F}_z^2$, respectively. The former part induces the Larmor precession, thus, to transform to the co-rotating frame an evolution

$$\hat{U}_L = e^{i\hat{\mathcal{H}}_{B,0}t/\hbar} \quad (3.5)$$

with inverted sign is applied. In the Larmor frame a Schrödinger picture state $|\Psi_S\rangle$ that includes the time evolution with $\hat{\mathcal{H}}_B$ as time dependence is written as $|\Psi_L\rangle = \hat{U}_L |\Psi_S\rangle$. From this, the Schrödinger equation in the rotating frame can be

derived as

$$\begin{aligned} i\hbar \frac{\partial}{\partial t} |\Psi_L\rangle &= i\hbar \left(\frac{\partial}{\partial t} \hat{U}_L \right) |\Psi_S\rangle + \hat{U}_L \left(i\hbar \frac{\partial}{\partial t} |\Psi_S\rangle \right) = \hat{U}_L \left(-\hat{\mathcal{H}}_{B,0} + \hat{\mathcal{H}} \right) |\Psi_S\rangle \\ &= \hat{\mathcal{H}}'_B \hat{U}_L |\Psi_S\rangle = \hat{\mathcal{H}}'_B |\Psi_L\rangle, \end{aligned} \quad (3.6)$$

where we used $[\hat{\mathcal{H}}_{B,0}, \hat{\mathcal{H}}'_B] = 0$ because the Hamiltonians exclusively contain powers of \hat{F}_z . Thus, the time evolution in the rotating frame is given by just the second-order Zeeman contribution $\hat{\mathcal{H}}'_B$. Experimentally, this transformation to the co-rotating frame corresponds to evolving the phase φ from eq. (3.1) of RF (and MW) couplings with the Larmor frequency p .

At this point, the remaining second-order Zeeman shift introduces an equal energy offset for both side modes $m_F = \pm 1$. Its Hamiltonian can also be written in terms of the \hat{Q}_{zz} operator

$$\hat{\mathcal{H}}'_B = \hbar q (\hat{n}_1 + \hat{n}_{-1}) = \hbar q \frac{\hat{Q}_{zz}}{2} + \text{const.} \quad (3.7)$$

by introducing an energy offset of $2/3 \hbar q$ to all sublevels which can be neglected as overall phase. Thus, eq. (3.7) shows that an external magnetic field implements exactly the rotation of a spin state with \hat{Q}_{zz} when considering the spin-1 system in the Larmor frame.

Additional to this method, \hat{Q}_{zz} can also be implemented by shifting the energy of the $m_F = 0$ level via off-resonant MW dressing. [18] This can be achieved by, for instance, coupling the levels $|1, 0\rangle \leftrightarrow |2, 0\rangle$ with a MW frequency being red-detuned by δ to the transition. Considering an off-resonant two-level Rabi coupling between the aforementioned sublevels, the resulting Hamiltonian in the Larmor frame of an external magnetic field is given by

$$\hat{\mathcal{H}}'_B = \hbar \left(q + \frac{\Omega_{\text{MW}}^2}{2\delta} \right) \frac{\hat{Q}_{zz}}{2} + \text{const.}, \quad (3.8)$$

where Ω_{MW} is the corresponding MW Rabi frequency. Consequently, the time required for \hat{Q}_{zz} rotations can be decreased by applying MW dressing. Thus, limiting the off-resonant transfer amplitude to 10^{-3} and assuming a typical experimental Rabi frequency of $\Omega_{\text{MW}} \approx 9$ kHz, the additional MW-dressing allows an increase of the coupling frequency to about $3.5q$.

To develop a better understanding of the time evolution with this operator let us consider the example of a fully elongated spin in the transversal plane, e.g. an \hat{F}_x eigenstate with full length: $\Psi \sim (1/2, 1/\sqrt{2}, 1/2)^T$. Using the spinor notation

$$\Psi = \begin{pmatrix} \Psi_1 \\ \Psi_0 \\ \Psi_{-1} \end{pmatrix} = \begin{pmatrix} \sqrt{n_1} e^{i\varphi_1} \\ \sqrt{n_0} e^{i\varphi_0} \\ \sqrt{n_{-1}} e^{i\varphi_{-1}} \end{pmatrix} \quad (3.9)$$

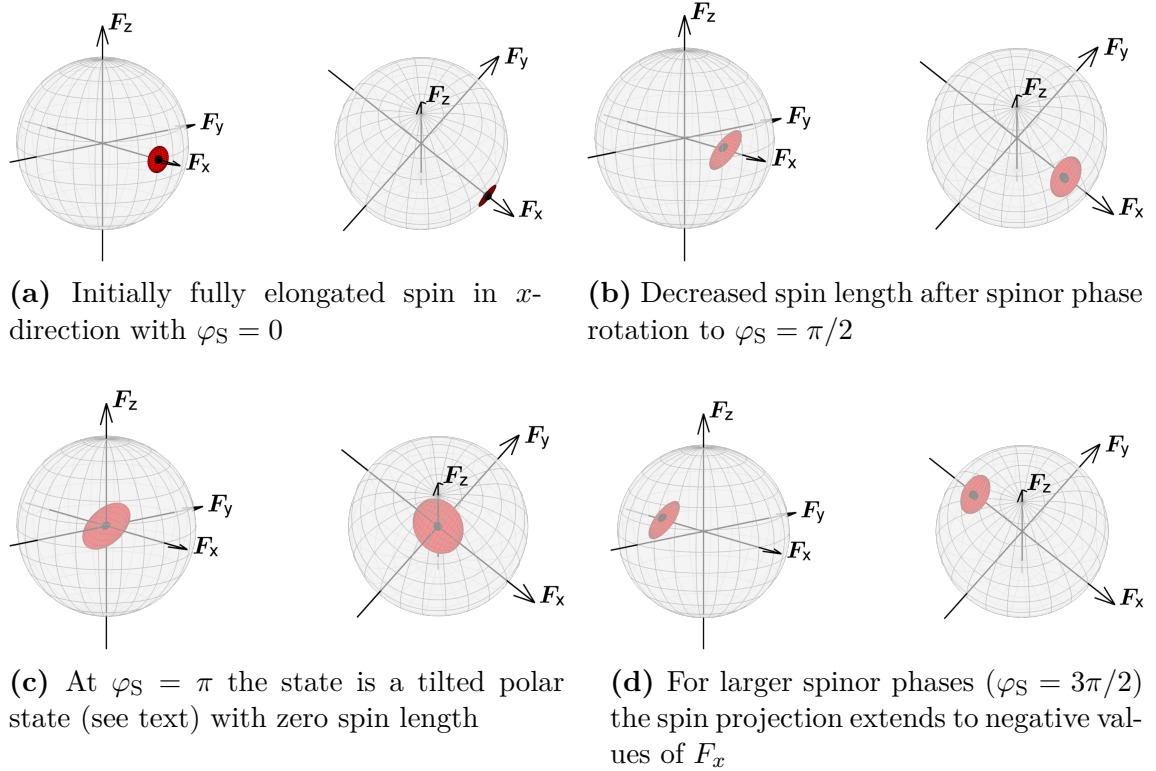


Figure 3.4: Evolution of an fully elongated spin in x -direction under second-order Zeeman shift (in the Larmor frame) displayed in the spin sphere. The red ellipsoids show the fluctuations of the corresponding states in all spatial directions (computed via eq. (2.8)) for $N = 10$ atoms. Complementary, the centre of the fluctuation ellipsoid (black dot) marks the spin dipole expectation value. The evolution of the state is shown in steps of $\pi/2$ in the spinor phase. Initially (a), the fully elongated spin in x -direction ($\varphi_S = 0$) shows small fluctuations transversal to the spin direction. By increasing the spinor phase to $\varphi_S = \pi/2$ (b) the dipole projections (“spin length”) reduces while the fluctuations quickly transform to contain the largest contributions in a plane titled by 45° around x against the transversal plane. For $\varphi_S = \pi$ (c) the spin length vanishes and the fluctuations lie entirely in the tilted plane. Thus, this resembles a fully aligned state. Continuing the phase evolution beyond this point ($\varphi_S = 3\pi/2$), the spin projection extends to negative x -direction (d). Afterwards, the state will continue its oscillation; first arriving at a fully elongated spin antiparallel to x at $\varphi_S = \pi$ before arriving at the initial state again for $\varphi_S = 4\pi$. During the whole evolution the spin projection in y - and z -directions remain zero.

with normalisation $n^2 = n_1^2 + n_0^2 + n_{-1}^2$ these states are characterised by sublevel amplitudes $n_1 = n_{-1} = n/4$ and $n_0 = n/2$. Recalling the coupling matrices of the linear and second-order Zeeman shifts, we also see that the magnetic field acts symmetrically on the side mode phases: $\varphi_{\pm 1} = \varphi_q \pm \varphi_L$, where $\varphi_q = qt$ and $\varphi_L = pt$. Next, by applying the mean-field approximation for large occupations n_i (see section 2.2) to replace the field operators $\hat{\Psi}_i$ by the spinor fields Ψ_i from eq. (3.9) the expectation values of the for the transversal spin operators can be calculated to be

$$\begin{aligned} F_x &= \sin(\varphi_L) \cos(\varphi_S/2) \\ F_y &= \cos(\varphi_L) \cos(\varphi_S/2). \end{aligned} \tag{3.10}$$

Here, we normalised the expectation values with n to a maximum of 1 and use the Larmor phase $\varphi_L = (\varphi_1 - \varphi_{-1})/2$ that characterises the phase evolution under the linear Zeeman shift. Further the spinor phase $\varphi_S = \varphi_1 + \varphi_{-1} - 2\varphi_0$ is introduced to quantify the relative phase evolution between zero and side modes. [8] From the definition of these two representations of the spin-1 phases it is clear that the Larmor contribution φ_L is evolved exclusively by the linear Zeeman shift, while the spinor phase φ_S only depends on the second-order effect via $\varphi_S = 2qt$. Finally, from eq. (3.10) we see that the Larmor phase induces a rotation of the spin expectation value in the transversal plane as is expected for the spin precession in an external magnetic field. Furthermore, the spinor phase evolution driven by \hat{Q}_{zz} induces an oscillation of the total spin length $|F_{\perp}| = \sqrt{F_x^2 + F_y^2} = n|\cos(\varphi_S/2)|$.

In fig. 3.4 different stages in the spinor phase evolution are shown inside the spin sphere. Here, since the state is chosen to have full spin length in the plane, the initial spinor phase is zero. By evolving φ_S in steps of $\pi/4$ in the co-rotating Larmor frame the spin length decreases along the initial spin axis x . During this evolution the initial coherent fluctuation disk starts to extend also in the diagonal plane until the fluctuations form a disk again within this plane for $\varphi_S = \pi/2$. At this point the spin length has also reduced to zero. These two properties are main features of a tilted polar state, which will be addressed in more detail below. Continuing the phase evolution further builds up a negative spin projection along x . As we have seen from the spin expectation values this oscillation will continue further and returns to the initial F_x eigenstate for $\varphi_S = 4\pi$.

Experimentally, not only a fully elongated spin state but also the polar state $\Psi \sim (0, 1, 0)^T$ can be accessed by fast coupling pulses. Besides a vanishing spin length this state possesses fluctuations only in the x - y -plane (fluctuation disk). Spin-dipole rotations, as can be seen in fig. 3.3, rotate not only the expectation value \mathbf{F} but also the fluctuation eigenvectors. From this we can understand that the state displayed in fig. 3.4c corresponds to such a polar state whose fluctuation disk is rotated around the x -axis. The corresponding spin-dipole rotations around a transversal axis drive population transfers between zero and side modes via terms like $\hat{\Psi}_0^\dagger(\hat{\Psi}_1 + \hat{\Psi}_{-1})$. This couples the zero with the side modes, which consequently drives population transfers between the levels. Explicitly evaluating the process,

rotating the polar state by an angle ϑ builds up the side mode population according to $n_{\pm 1} \sim \sin^2(\vartheta)/2$. Starting from this tilted polar state we can again investigate a subsequent spinor phase evolution. From Inserting the new normalisation condition into the calculation leading to eq. (3.10) the spin length for this new scenario can be obtained as

$$|F_{\perp}| = |\sin(2\vartheta) \sin(\varphi_S/2)|. \quad (3.11)$$

In this equation φ_S specifies the spinor phase accumulated after preparation of the initial state. The dependence on this phase is given by a sine because the tilt of the polar already introduces a phase offset $\varphi_S = \pi$. This results from the prefactor of the spinor side modes introduced by the spin-dipole rotation.

Thus, by starting from both an elongated transversal spin or a polar state a spin with controlled amplitude can be implemented. The change in spin length is driven by a spinor phase evolution due to the second-order Zeeman shift in an external magnetic field. Later, we will implement both of these methods to generate specific spin lengths.

3.3.2 Readout of $\langle \hat{Q}_{xz} \rangle$ and $\langle \hat{Q}_{yz} \rangle$

The next quadrupoles we want to consider are \hat{Q}_{xz} and \hat{Q}_{yz} . These, in contrast to \hat{Q}_{zz} , contain coherences between all magnetic sublevels and are similar to the transversal dipole operators \hat{F}_y and \hat{F}_x . Since the treatment of the second pair of operators is completely analogous to $(\hat{F}_x, \hat{Q}_{yz})$, here the discussion is limited to these two operators. To illustrate their connection, let us consider

$$\hat{F}(\theta) := \frac{e^{i\theta/2}}{\sqrt{2}} \hat{\Psi}_0^\dagger (\hat{\Psi}_1 + \hat{\Psi}_{-1}) + h.c.. \quad (3.12)$$

For $\theta = 0$ this is the dipole operator $\hat{F}(0) = \hat{F}_x$ and for a phase of π it becomes the quadrupole $\hat{F}(\pi) = \hat{Q}_{yz}$. Since $\hat{\Psi}_0$ appears in each of the terms the prefactor $e^{i\theta/2}$ can be linked with the phase of the $m_F = 0$ component. This relative phase accumulation between the zero and side modes is equivalent to a spinor phase evolution by $\varphi_S = \pi$. At the end of the previous section we have seen that this corresponds to the action of \hat{Q}_{zz} , i.e. the second-order Zeeman shift. Thus, one expects to obtain the quadrupole observable \hat{Q}_{yz} if first evolving the spinor phase by π and afterwards mapping the dipole direction \hat{F}_x to the quantisation axis z (see fig. 3.5). Explicitly, these scheme can be verified by calculating

$$\langle \hat{Q}_{xz} \rangle = \left\langle e^{i\frac{\pi}{2}(\hat{n}_1 + \hat{n}_{-1})} e^{i\frac{\pi}{2}\hat{F}_x} \hat{F}_z e^{-i\frac{\pi}{2}\hat{F}_x} e^{-i\frac{\pi}{2}(\hat{n}_1 + \hat{n}_{-1})} \right\rangle, \quad (3.13)$$

Here, the equivalent expression for \hat{Q}_{xz} is obtained by replacing $\hat{F}_x \rightarrow \hat{F}_y$ in eq. (3.13). We see that by building on spinor phase rotations from section 3.3.1 and mappings of spin dipoles to the readout direction from section 3.2 even more observables of the spin-1 system become accessible.

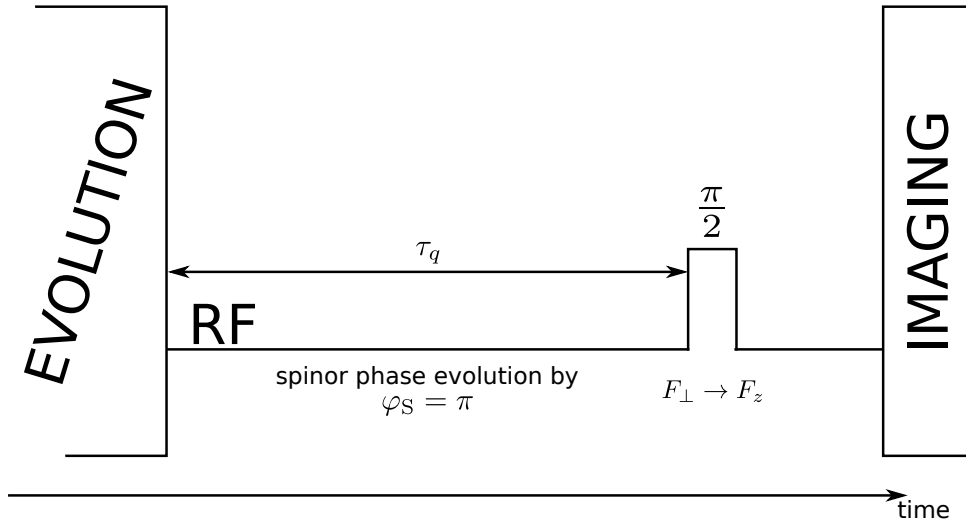


Figure 3.5: Schematic sequence for the experimental implementation of \hat{Q}_{yz} or \hat{Q}_{xz} read-out. After the evolution period the system is held in a constant external magnetic field to generate a spinor phase evolution by $\varphi_S = 2q\tau_q$. This step maps the quadrupole to the transversal dipole operators. Thus, by a subsequent RF $\pi/2$ -pulse their projections are extracted by imaging the sublevel densities and inferring F_z . After this mapping scheme the extracted value resembles a measurement of projection onto the corresponding quadrupole.

3.3.3 Readout of $\langle \hat{Q}_{xy} \rangle$ and $\langle \hat{Q}_{y^2-x^2} \rangle$

Now we turn to operators which, require a different approach for reading out their expectation values. Here, the observables of interest have the form

$$\hat{Q}_{xy} = \begin{pmatrix} 0 & 0 & -i \\ 0 & 0 & 0 \\ i & 0 & 0 \end{pmatrix} \quad \text{and} \quad \hat{Q}_{y^2-x^2} = \begin{pmatrix} 0 & 0 & -1 \\ 0 & 0 & 0 \\ -1 & 0 & 0 \end{pmatrix}, \quad (3.14)$$

which shows that these operators only contain coherences between the side modes $m_F = \pm 1$. Recalling the spin dipole rotations from section 3.2, these can be implemented by coupling different sublevels via oscillating magnetic fields. Further, by removing the central line and column from the matrices we see that these operators are essentially the x and y Pauli matrices from eq. (2.2). Thus, in analogy to a spin-1/2 system, the couplings which need to be implemented are those of a two-level system. Here, this system is composed of only the $m_F = \pm 1$ levels, thus the zero mode is not allowed to be coupled to any of the other levels. Consequently, the usage of an ancilla level in the $F = 2$ manifold is required to either shelve the one level or allow direct two-level coupling of the side modes. This again allows for two schemes: applying MW or RF pulses to achieve mixing of the spin side modes.

First, we consider MW-coupling to access the coherences. The pulse sequence implementing this readout (see fig. 3.6a) first transfers the total $|1, -1\rangle$ population to $|2, 0\rangle$ by a MW π -pulse. Then, another coupling implements the $\pi/2$ -mixing of $|2, 0\rangle \leftrightarrow |1, 1\rangle$, before reversing of the initial population transfer. Here, by interpreting the $\pi/2$ mixing pulse in the spin-1/2 picture, this process can be regarded as a spin rotation. Thus, this shows that by changing the phase of the mixing pulse (i.e. tilting the rotation axis) by $\pi/2$ we can switch between readout of \hat{Q}_{xy} (corresponding to $\hat{\sigma}_x$) and $\hat{Q}_{y^2-x^2}$ (corresponding to $\hat{\sigma}_y$). Furthermore, this approach also provides information about the quantities which have to be extracted in this scheme. As for the usual spin mappings from the transversal directions to the z -axis the relevant quantity is the z -spin in the $m_F = \pm 1$ subsystem. Here, this corresponds to the usual spin F_z .

Explicitly, these sequences can be proven by extending the spherical basis we usually apply to describe the $F = 1$ manifold by the state $|2, 0\rangle$: $(a, b, c, d)^T = a|1, 1\rangle + b|1, 0\rangle + c|1, -1\rangle + d|2, 0\rangle$. With this, the Hamiltonians $\hat{\mathcal{H}}_1$ of the transfer $|1, 1\rangle \leftrightarrow |2, 0\rangle$ and $\hat{\mathcal{H}}_2$ of the mixing pulse can be represented as

$$\hat{\mathcal{H}}_1 = \frac{1}{2} \begin{pmatrix} 0 & 0 & 0 & 1 \\ 0 & 0 & 0 & 0 \\ 0 & 0 & 0 & 0 \\ 1 & 0 & 0 & 0 \end{pmatrix} \quad \text{and} \quad \hat{\mathcal{H}}_2(\varphi) = \frac{1}{2} \begin{pmatrix} 0 & 0 & 0 & 0 \\ 0 & 0 & 0 & 0 \\ 0 & 0 & 0 & e^{i\varphi} \\ 0 & 0 & e^{-i\varphi} & 0 \end{pmatrix}, \quad (3.15)$$

where φ is the relative MW phase between the first and second pulse in the rotating Larmor frame. Using this and also extending the quadrupole matrices to this basis,

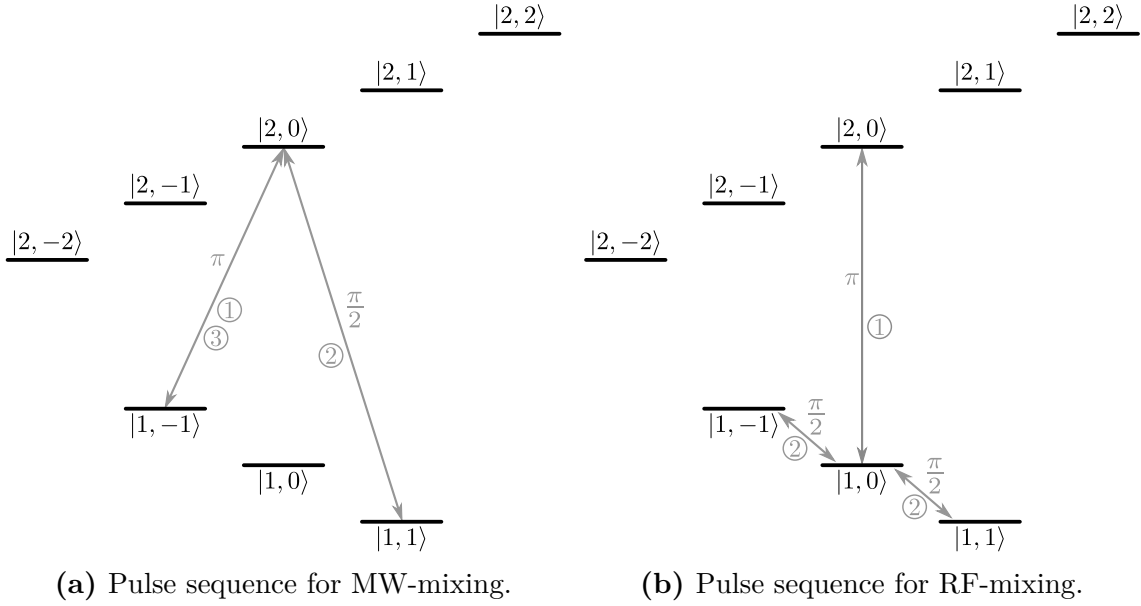


Figure 3.6: MW- and RF-pulse sequences for the read-out of \hat{Q}_{xy} and $\hat{Q}_{y^2-x^2}$. The circled numbers mark the chronological order of the pulses. In both cases the phase of the $\pi/2$ mixing pulses determines which of the quadrupole operators is extracted (see text). **a)** First, a MW π -pulse transfers the population from the level $|1, -1\rangle$ to $|2, 0\rangle$. Then, a $\pi/2$ -pulse induces mixing with $|1, 1\rangle$ before the same π -pulse transfers the population back to $|1, -1\rangle$. **b)** Initially, the zero mode atoms are shelved in $|2, 0\rangle$ by a MW π -pulse. Subsequently, a RF $\pi/2$ -pulse mixes the side modes.

the following relations can be verified:

$$\begin{aligned}\langle \hat{Q}_{xy} \rangle &= \left\langle e^{i\pi\hat{\mathcal{H}}_1} e^{i\frac{\pi}{2}\hat{\mathcal{H}}_2(\frac{\pi}{2})} e^{i\pi\hat{\mathcal{H}}_1} \hat{F}_z e^{-i\pi\hat{\mathcal{H}}_1} e^{-i\frac{\pi}{2}\hat{\mathcal{H}}_2(\frac{\pi}{2})} e^{-i\pi\hat{\mathcal{H}}_1} \right\rangle, \\ \langle \hat{Q}_{y^2-x^2} \rangle &= - \left\langle e^{i\pi\hat{\mathcal{H}}_1} e^{i\frac{\pi}{2}\hat{\mathcal{H}}_2(0)} e^{i\pi\hat{\mathcal{H}}_1} \hat{F}_z e^{-i\pi\hat{\mathcal{H}}_1} e^{-i\frac{\pi}{2}\hat{\mathcal{H}}_2(0)} e^{-i\pi\hat{\mathcal{H}}_1} \right\rangle.\end{aligned}\tag{3.16}$$

Thus, these quadrupole coherences can be extracted by direct MW-coupling of the corresponding sublevels, where the phase of the MW-pulses selects between the two operators.

Instead of MW-coupling also a RF pulse can be used to mix the side modes. However, from eq. (3.1) we can see that this coupling, via the perpendicular spin dipole operators, also generates mixing with the $m_F = 0$ mode. To avoid this, the population of the zero mode can be shelved to $|2, 0\rangle$ for the duration of the RF coupling. Thus, following the MW π -pulse resonant to $|1, 0\rangle \leftrightarrow |2, 0\rangle$ a RF $\pi/2$ -pulse is applied to mix the side modes (see fig. 3.6b for the full pulse scheme). In this case, however, because the RF-mixing also involves the zero mode the spin-1/2 picture of a two level system is not applicable here. Consequently, instead of \hat{F}_z another quantity must be extracted from the densities after the mapping scheme: $\rho_0 = n_0 - (n_1 + n_{-1})$, or in operator form

$$\hat{\rho}_0 := 2\hat{n}_0 - \mathbb{1} = \begin{pmatrix} -1 & 0 & 0 \\ 0 & 1 & 0 \\ 0 & 0 & -1 \end{pmatrix}.\tag{3.17}$$

Furthermore, also the phases of the RF-pulse must be chosen differently than previously: $-\pi/4$ for \hat{Q}_{xy} and $\pi/2$ for $\hat{Q}_{y^2-x^2}$.

To check the equivalence of this method and the quadrupole expectation values it is useful to first introduce the projector onto the side modes

$$\hat{P}_{\pm 1} := \begin{pmatrix} 1 & 0 & 0 \\ 0 & 0 & 0 \\ 0 & 0 & 1 \end{pmatrix},\tag{3.18}$$

which effectively describes the shelving by removal of the $m_F = 0$ population from the $F = 1$ manifold. Neglecting the small \hat{F}_z term in eq. (3.1) we can now calculate

$$\begin{aligned}\langle \hat{Q}_{xy} \rangle &= \left\langle \hat{P}_{\pm 1} e^{i\frac{\pi}{2}\hat{\mathcal{H}}_{\text{RF}}(-\frac{\pi}{4})} \hat{\rho}_0 e^{-i\frac{\pi}{2}\hat{\mathcal{H}}_{\text{RF}}(-\frac{\pi}{4})} \hat{P}_{\pm 1} \right\rangle, \\ \langle \hat{Q}_{y^2-x^2} \rangle &= \left\langle \hat{P}_{\pm 1} e^{i\frac{\pi}{2}\hat{\mathcal{H}}_{\text{RF}}(\frac{\pi}{2})} \hat{\rho}_0 e^{-i\frac{\pi}{2}\hat{\mathcal{H}}_{\text{RF}}(\frac{\pi}{2})} \hat{P}_{\pm 1} \right\rangle.\end{aligned}\tag{3.19}$$

Thus, this scheme allows the read-out of the same quantities as the MW-only method.

4 Measurement of Quadrupole Rotations and Observables

So far, the concept of rotations in spin-space has been discussed. Here, measurements implementing these methods for either state preparation or read-out are presented. Utilising the dynamics in an external magnetic field, the spinor phase evolution of states with different transversal spin lengths is observed. The results obtained there, in turn, are applied to engineer a spin wave in space. Furthermore, following a quench in of the side-mode detuning after long-time evolution quadrupole observables are measured to investigate the loss of spin length at late times.

4.1 Spinor Phase Evolution of Transversal Spin

In an external magnetic field a spin-1 system is subject to first and second-order Zeeman shifts p and q , resulting in an accumulation of Larmor and spinor phase, respectively. As we have seen in section 3.3.1 the spinor phase evolution of states in the transversal plane results in an oscillating spin length. Meanwhile, in the experiment the Larmor precession is taken into account by evolving the phase of the RF-pulses at the corresponding frequency. For short evolution times. In principle, this should allow the readout of not only the spin length but also the direction in the transversal plane. However, we will see that fluctuations in the magnetic field strength hinder this extraction.

To experimentally probe the spin length oscillations induced by changes in the spinor phase via the second-order Zeeman shift two different initial conditions are used. Starting from a fully elongated spin in x -direction the oscillation of spin length with evolution time is extracted. In a second measurement, zero-length states with different rotation angles are transformed by a spinor phase rotation of constant duration.

Spinor Phase Evolution of an Elongated Spin

We start with the case of an initially fully elongated transversal spin. For this experiment, ca. 56 000 atoms are loaded into the crossed dipole trap. Compared to the elongated waveguide potential introduced in section 3.1 the longitudinal confinement is increased to minimise the effect of spatial magnetic field gradients. First, an elongated transversal spin is produced from the initial BEC in $|1, -1\rangle$ by a RF $\pi/2$ -rotation. Because the initial Larmor phase cannot be extracted experimentally the absolute rotation axis of the first pulse is unknown. However, due to the rotational

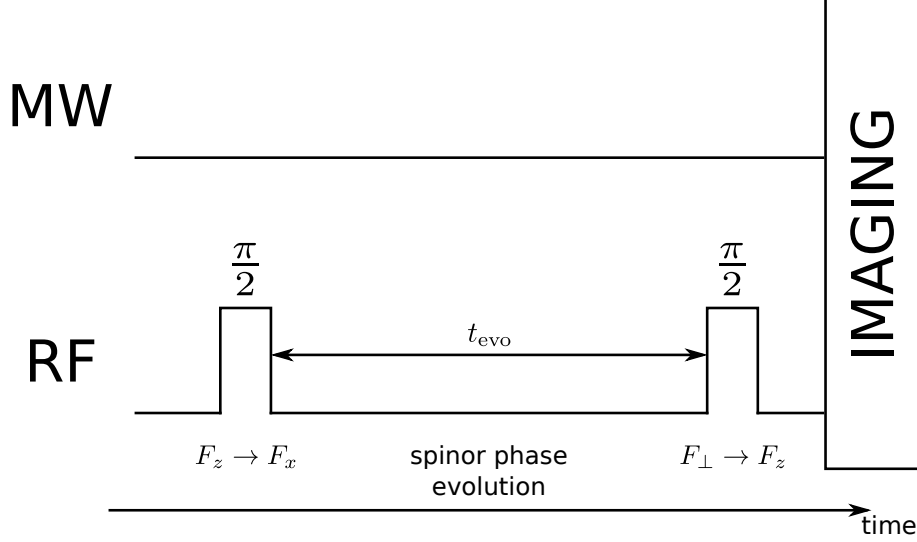


Figure 4.1: Schematic overview of the pulse sequence for observing the spinor phase rotation of an elongated spin oriented perpendicular to the \mathbf{B} axis. The first RF pulse rotates the initially fully polarised spins from the z -axis to the x - y -plane. Subsequently, the spinor phase evolves for a certain amount of time t_{evo} due to the second order Zeeman shift. Finally, before readout another RF-pulse maps a transversal spin direction to the quantisation axis for Stern-Gerlach readout during the imaging sequence. Here, the relative phase between the two RF-pulses allows the selection of the readout direction (see text).

symmetry around the magnetic field axis only the relative phase between initial and read-out direction in the transversal plane is of interest for the spin dynamics. Thus, the initial rotation axis can be defined as F_y to fix a coordinate system for the following discussion.

After the first RF-coupling of duration $\tau_{\pi/2}^{\text{RF}} = 14.3 \mu\text{s}$, the system evolves for the time interval t_{evo} in an external magnetic field of $B = 0.884 \text{ G}$ (see fig. 4.1 for the full experimental sequence). Starting with the spinor phase $\varphi_S = \varphi_1 + \varphi_{-1} - 2\varphi_0 = 0$, during the evolution time the state picks up the phase $\varphi_S = 2qt_{\text{evo}}$ (see section 3.3.1). In the experiment the system is evolved for up to $t_{\text{evo}} = 18 \text{ ms}$ and afterwards a second RF-pulse enables the extraction of the transversal spin. Here, by controlling the relative phase φ between the two RF-signals the read-out direction is set (see eq. (3.1)). In the co-rotating Larmor frame the introduction of this phase shift rotates the read-out axis by an angle φ around the z -axis. Thus, $\varphi = 0$ corresponds to the extraction of F_x and $\varphi = \pi/2$ accesses F_y .

After mapping to the z -basis the transversal spin projection is inferred from the atom numbers N_m in the magnetic sublevels m_F . Values for N_m are extracted by associating each Stern-Gerlach-separated cloud of atoms to the corresponding sublevel and summing the atom numbers obtained for each pixel in this region. Then, the normalised z -projection is obtained with $F_z = (N_1 - N_{-1}) / (N_1 + N_0 + N_{-1})$.

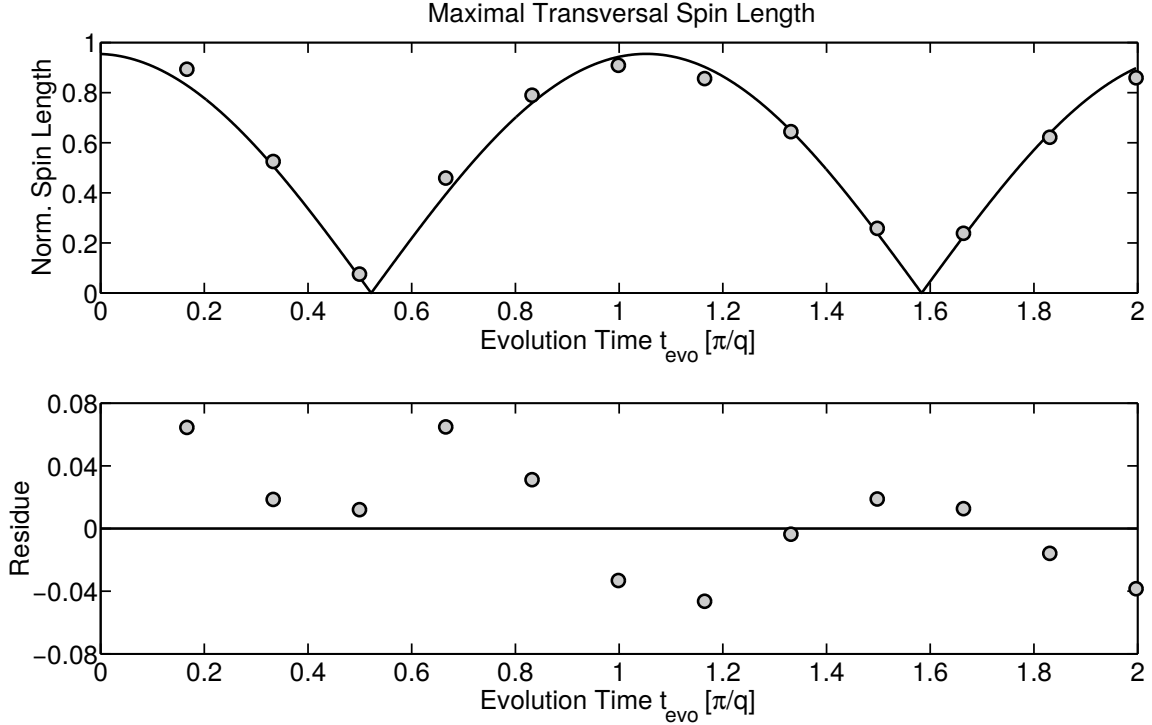


Figure 4.2: After initialisation of a fully elongated transversal spin and subsequent spinor phase evolution for the period t_{evo} the spin length projected on equally sampled transversal directions is extracted. Here, the spinor phase evolution is implemented by a second-order Zeeman shift of $q \approx 2\pi \times 55.9$ Hz. Across the set of all realisations with the same t_{evo} the maximum length is extracted and plotted against evolution time (grey dots). The solid curve displays the best fit of eq. (4.1) with amplitude, phase, and frequency as free parameters. Within its errors the phase extracted by the optimisation is zero but the oscillation frequency from the second order Zeeman shift by about 3 Hz.

For the first analysis procedure the maximal spin length is extracted from the set of realisations prepared with the same evolution time t_{evo} . Figure 4.2 shows these values as function of t_{evo} .

To describe the transversal spin length, a function of the form

$$|F_{\perp}|(t) = |A \cos(q_{\text{eff}}t_{\text{evo}} + \varphi)| \quad (4.1)$$

is used. To compare the oscillation in the spin length with the expectation from the Hamiltonian (3.7) the parameters of eq. (4.1) are extracted by a fit to the data (solid line in the upper plot of fig. 4.2). The phase offset extracted by the optimisation is $\varphi = (0.03 \pm 0.04)\pi$. This agrees the expectation of a vanishing value when assuming an initial spin length of $|F_{\perp}| = 1$. While in section 3.3.1 the spin length is predicted to oscillate with $q \approx 2\pi \times 56.2$ Hz, the fit value $q_{\text{eff}} = 2\pi \times (52.9 \pm 0.6)$ Hz is smaller by $\Delta q \approx 2\pi \times 3.3$ Hz. This deviation may be introduced by mean field shifts of the magnetic sublevels. Equation (2.15) shows that when writing the spin-spin

interaction in terms of the field operators five terms arise which only contain sublevel populations. All of them contain the side mode populations but only two depend on $m_F = 0$. Assuming the sublevel densities of a fully elongated transversal spin $n_1 = n_{-1} = n_0/2$ (see section 3.3.1) and taking into account the prefactors of the spin-spin energy a larger shift for the side modes may be expected in a mean-field approximation. This shift, due to the negative sign of c_1 will reduce the frequency of the spinor phase evolution, which would result in a reduced q_{eff} . Additional to the reduction in frequency, also the oscillation amplitude $A = 0.96 \pm 0.02$ shows a deviation from the full modulation amplitude expected for the spin length $|F_{\perp}| = 1$. This may originate from a decay in the oscillation amplitude with time. However, the fit residue in fig. 4.2 does not indicate a clear trend supporting this scenario. Thus, also a reduced but constant spin length is compatible with the data. While the former case is not captured by the spin dynamics presented here, a reduced amplitude is explainable by a deviation of the RF-pulse duration from the exact time required for a $\pi/2$ -pulse. Here, an error of $\sim 2.5 \mu\text{s}$ would explain the measured amplitude.

In the experiment the second RF-pulse was generated with 12 equally spaced phases between $\varphi = 0$ and $\varphi = 11\pi/12$. This should allow the read-out of spin projection directions rotated by φ with respect to the F_x -axis in the transversal plane. Figure 4.3 shows the spin projections for the different read-out phases. Each scan of the phase was repeated five to ten times for every evolution time. Here, the projections are displayed colour-coded for each phase (x -axis of plot) and repetition (y -axis of plot). For the shortest time $t_{\text{evo}} \approx 1.48 \text{ ms}$, corresponding to $\varphi_S \approx 0.33 \pi$, a sinusoidal modulation of the spin length with the readout direction is visible. This confirms the existence of a well-aligned spin along a fixed direction. However, the initial state was aligned to the F_x -axis which would corresponds to measuring the maximal value at an angle 0. Instead, the readout corresponds to a polar angle of $\theta = (0.68 \pm 0.01) \pi$. Here, the offset phase was estimated by a fit to the fringe obtained from all read-out phases φ while averaging the data for each φ over the first five repetitions. This phase shift may be induced by a residual magnetic field offset which can be estimated with $\Delta B = \theta / (\rho t_{\text{evo}}) B \approx 0.3 \text{ mG}$. However, this offset would reduce the modulation amplitude of MW-Rabi couplings which is not compatible with experimental observations. Thus, ΔB must be smaller than this value and consequently the phase shift in the read-out direction is not entirely induced by a magnetic field offset. Because over short time periods the read-out direction can be reproduced very well, which excludes the RF-electronics as source of this offset. As remaining possibility this leaves small drifts in the magnitude of the magnetic field on the time scale of $\sim 1 \text{ ms}$.

Furthermore, for the sixth repetition of the first evolution time this fringe phase changes. This is caused by a small adjustment of the magnetic field (see discussion of fig. 4.6). Here, by observing a Ramsey fringe for a coupling of $|1, -1\rangle \leftrightarrow |2, 0\rangle$ the magnetically induced shift of the former state can be measured. From the detuning of the transition frequency to the splitting at $B = 0.884 \text{ G}$ the accumulated drift in B is quantified and counteracted by adjusting the current through a set of bias field

coils accordingly.

The changes in the fringes for larger t_{evo} show that with increasing hold time the variations of the spin lengths from one experimental realisation to another increase. Because over a time scale of $t_{\text{evo}} \lesssim 1/(2q)$ the spin length oscillation agrees well with a variation of constant amplitude (see fig. 4.1) it can be assumed that the oscillation of the spin projection along the F_x -axis is still valid. Instead, short-term fluctuations in the magnetic field strength scramble the transversal readout direction. Thus, the varying B induces a slightly different linear Zeeman shift than assumed by the experimental control. Consequently, the RF-signal accumulates a phase error which results in a tilted read-out axis.

Control of Spin Length via Spinor Phase Evolution of a Tilted Polar State

The second experiment utilising spinor phase evolutions with \hat{Q}_{zz} minimises the influence of magnetic field fluctuations by keeping the evolution times as short as possible. Here, the experiments are carried out with $\sim 72\,000$ atoms in the elongated waveguide potential described in section 3.1. Nevertheless, the inference of the spin projections is performed analogously to the previous measurement. Starting from a state with zero spin length an elongated spin is created by a spinor phase evolution of $\varphi_S = \pi$, as already introduced in section 3.3.1. Experimentally, first a polar state $\Psi = (0, 1, 0)^T$ is prepared by two MW π -transfers $|1, -1\rangle \rightarrow |2, 0\rangle \rightarrow |1, 0\rangle$ (see pulse sequence in fig. 4.4). Since this state only accumulates an overall phase under \hat{Q}_{zz} , next the side modes are populated by a RF-coupling of duration t_{RF} . Equivalently, this can be interpreted as a rotation of the polar state around a transversal axis by an angle θ_{RF} (see fig. 3.4c for a visualisation of $\theta_{\text{RF}} = 45^\circ$). Afterwards, the evolving spinor phase generates spin length in the direction of the initial tilt axis. Analogous to the previous measurement multiple transversal spin projections are extracted by a second phase-locked RF-pulse. Here, the initial tilt axis is defined as the x -direction and the read-out projection addressed by the second RF-pulse is specified by the polar angle φ in the transversal plane, where $\varphi = 0$ specifies the initial x -direction.

First let us investigate the prediction of the spin length along the x -axis after the application of this procedure. This value can be calculated by an application of the RF-pulses described above to the polar state $|\Psi\rangle$. Since the initial rotation angle θ_{RF} is scanned in this measurement, we explicitly take the first RF rotation into account when calculating the time evolution:

$$\langle \hat{F}_x \rangle (\theta_{\text{RF}}) = \langle \Psi | e^{i\theta_{\text{RF}} \hat{F}_x} e^{i\frac{\pi}{2} \hat{Q}_{zz}} \hat{F}_x e^{-i\frac{\pi}{2} \hat{Q}_{zz}} e^{-i\theta_{\text{RF}} \hat{F}_x} | \Psi \rangle = -\sin(2\theta_{\text{RF}}). \quad (4.2)$$

Here, the angle $\theta_{\text{RF}} = \Omega_{\text{RF}} t_{\text{RF}}$ with RF Rabi frequency $\Omega_{\text{RF}} = 2\pi \times (17.5 \pm 0.2)$ kHz is experimentally controlled by the coupling time of the initial RF pulse.

Applying the same analysis as previously, the maximum spin length across all readout directions in the transversal plane (shown in fig. 4.5) is evaluated. Here,

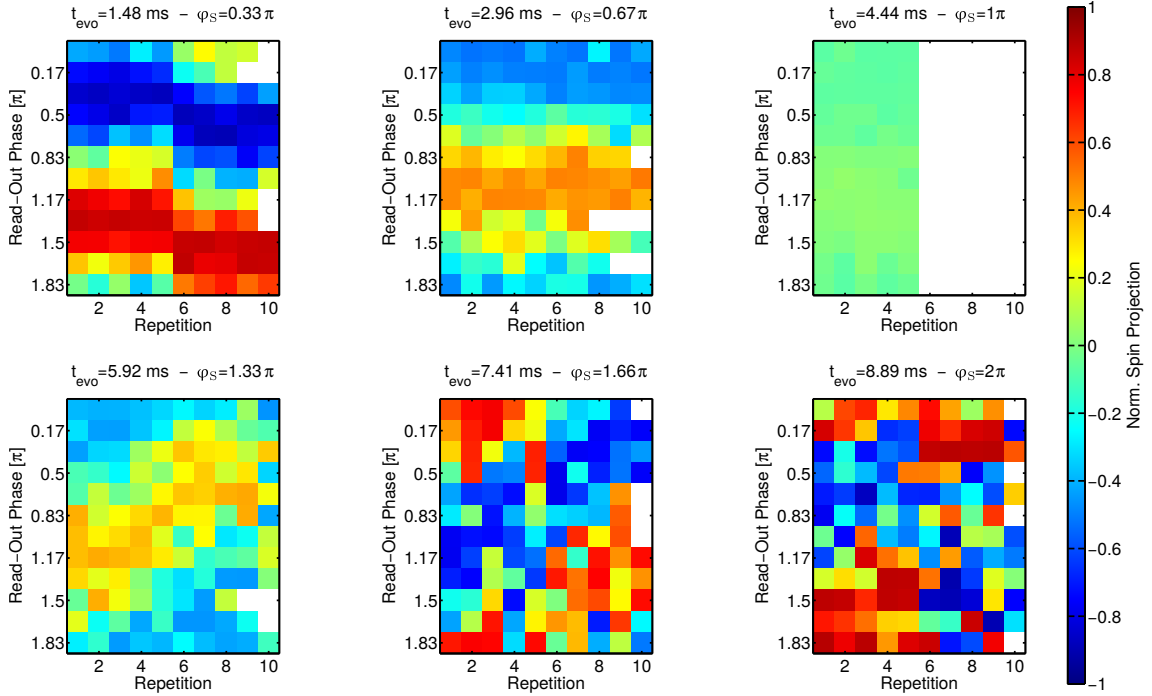


Figure 4.3: Spin projections (colour-coded) after spinor phase evolution of duration t_{evo} by the second-order Zeeman shift in an external magnetic field. For each graph the vertical axis specifies the phase of the second RF-pulse and horizontally the number of the experimental repetition is indicated. Scanning the phase of the read-out pulse rotates the projection direction in the transversal plane. This generates the fringe structure in vertical direction of the first plot ($t_{\text{evo}} = 1.48$ ms), which is compatible with a well-defined spin direction, as expected for a coherent preparation procedure. Due to a non-zero offset of the magnetic field the maximal spin length does not coincide with the initial spin direction F_x (read-out phase zero). With increasing evolution time a variation of the spin length is visible, which is induced by the spinor phase evolution (see fig. 4.2). However, for increasing t_{evo} the fringe structure becomes increasingly scrambled. The origin for this are fluctuations in the magnetic field amplitude which lead to fluctuations in the read-out phase and thus a varying spin projection direction in the transversal plane. White data points correspond to realisations which were filtered out due to exceptionally large deviations in the total atom number or malfunctions in the experimental control. For $t_{\text{evo}} = 4.44$ ms only five fringes were recorded.

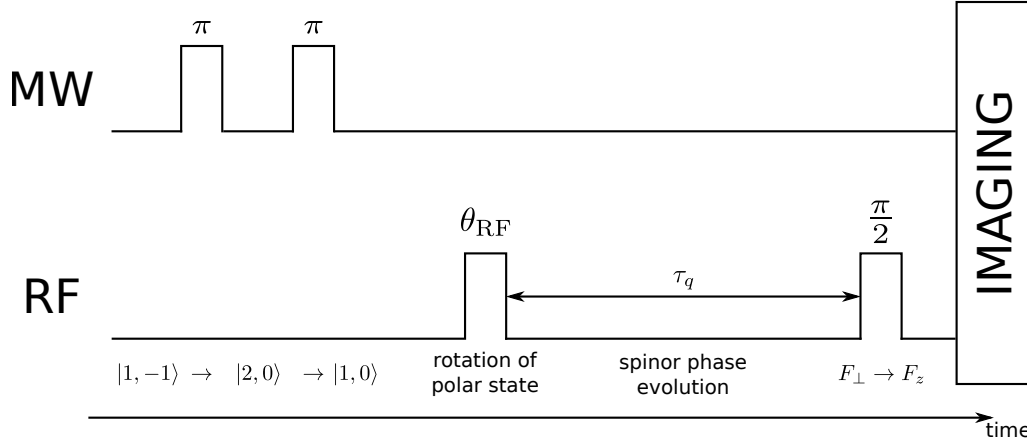


Figure 4.4: Schematic overview of the MW and RF pulse sequences for measuring the transversal spin of a rotated polar state with subsequent spinor phase evolution by $\varphi_S = \pi$. The MW pulses initialise the atoms in the polar state $|1, 0\rangle$, which is then rotated by the angle θ_{RF} around an axis perpendicular to \mathbf{B} . Evolving this state with a second order Zeeman shift in an external magnetic field for a period $\tau_q = 2\pi/(2q)$ generates spin length in the transversal plane. For read-out a different spin projection is mapped onto the quantisation axis by another phase-locked RF $\pi/2$ -pulse.

the data is fitted with

$$|F_{\perp}|(t) = A |\sin(2\Omega t_{\text{RF}} + \varphi)|, \quad (4.3)$$

which is derived from eq. (4.2) such that Ω matches the RF Rabi frequency if the model provides a good description. The amplitude $A = 0.994 \pm 0.007$ and phase $\varphi = (0.00 \pm 0.01)\pi$ of the best fit show a perfect agreement with expected behaviour. Here, this resembles a fully modulated oscillation at $A = 1$ starting from an initial state without spin length (vanishing offset phase $\varphi = 0$ of the sine function). Further, the fit residue in fig. 4.5 shows no long-time trend, confirming that a spinor phase evolution by π ($\pi/2$ -rotation with \hat{Q}_{zz}) allows a well-controlled adjustment of the transversal spin length. However, comparing the frequency $\Omega = 2\pi \times (16.91 \pm 0.02)$ kHz obtained from the fit with the Rabi frequency Ω_{RF} used in the experiment reveals a deviation of $\Delta\Omega \approx 2\pi \times 0.6$ kHz. Because the value of Ω_{RF} was estimated from the duration of a $\pi/2$ -pulse a drift of Ω_{RF} over a period of less than $\tau_{\pi/2}^{\text{RF}}$ cannot be excluded. For example, a reduction of the RF-voltage amplitude by 2% over this time period may already explain the difference $\Delta\Omega$. Thus, the most plausible cause for the deviation of the fit frequency seems to be a fast change in the RF Rabi frequency, leading to an over-estimation of its value from the experimental parameters.

As before, additional to the spin length also its transversal orientation can be extracted. Figure 4.7 (top) shows two exemplary fringes from equivalently prepared states projected along 12 different transversal directions. From these sinusoidal fits

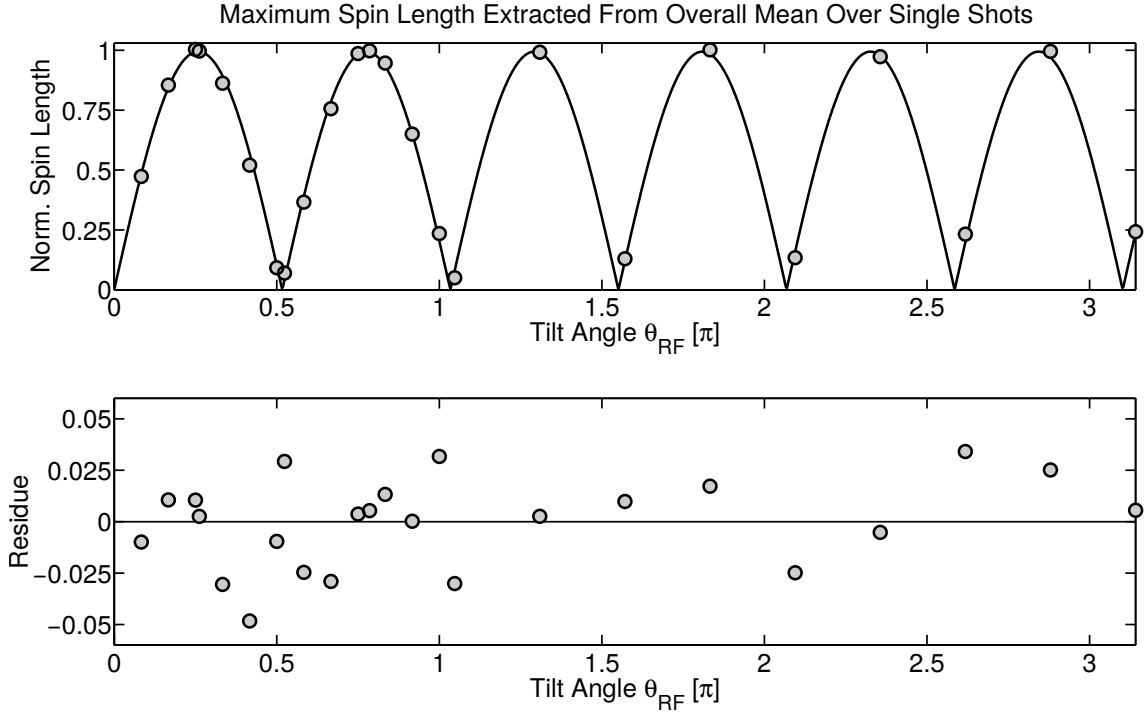


Figure 4.5: A polar state is first rotated by different angles θ_{RF} around a transversal axis and then its spinor phase is evolved by π . The upper plot shows the maximal transversal spin length across a set of spin projections with equally spaced read-out phase for each initial rotation angle θ_{RF} . As solid line the best fit of eq. (4.3) is displayed. The corresponding frequency $\Omega = (16.91 \pm 0.02)$ kHz lies close to the expected value of the RF Rabi frequency $\Omega_{RF} \approx 17.5$ kHz. In the lower half the residue of the fit is displayed.

the phases are extracted and phase jumps $\geq \pi$ between consecutive realisations are removed by adding $\pm 2\pi$ to reduce the step size. Plotting the phases in chronological order of their measurement in fig. 4.6 (top) shows many positions where the value suddenly changes while staying approximately constant before and after the jump. These sudden phase changes coincide with control measurements of the magnetic offset field (vertical dashed lines in the plot). At these points the magnitude of the field is measured and adjusted when required. This confirms the observation from before that the residual magnetic field changes from the adjustment procedure introduce significant Larmor phase errors in the RF-pulses. Due to small changes in the Larmor frequency the relative phase of the RF-rotations, even after an evolution time of just about 4ms, cannot be reproduced reliably over a long time of data taking. Thus, reading out absolute spin directions in the Larmor frame is not possible for such evolution times.

Even though no long-term stability of the read-out direction can be provided the magnetic field seems to be sufficiently stable to allow the read-out of relative direction in subsequent realisations over a time scale of a few minutes. Thus, fitting these fringes with a sinusoidal function of free amplitude provides another method to infer the spin length of the state. Averaging over all spin lengths obtained from equal experimental realisations and plotting the result in fig. 4.7 (centre) shows the same periodic structure as the evaluation of the maximum across the complete experimental sample (fig. 4.5). Applying the same function (4.3) as before, the phase and amplitude of the transversal spin length oscillation is extracted by a fit. Here, the offset phase $\varphi = (0.015 \pm 0.018)\pi$ agrees with a value of zero expected for the initially vanishing spin length. However, the normalised spin length of 0.91 ± 0.01 is smaller than the full amplitude of 1. This value corresponds to a spinor phase accumulation of π from a polar state rotated by 45° against the transversal plane (see eq. (3.11)). The reduction of the oscillation amplitude originates from fluctuations in the measurement. Constrained by the extraction method, no normalised spin values outside of the interval $[-1, 1]$ can be measured. Thus, fluctuations for spin values close to the bounds of this interval favour a reduced absolute value of the spin projection. Consequently, for large amplitudes almost any source of fluctuations reduces the inferred spin length, inducing a diminished amplitude of the fits. Here, the main source of fluctuations is the magnetic field, scrambling the Larmor phase, and thus tilting the read-out direction. Independent from these error sources, the RF Rabi frequency extracted from the periodicity of the fit should not be influenced by these error sources. However, the resulting value $\Omega = 2\pi \times (16.83 \pm 0.03)$ kHz shows a small deviation of $2\pi \times 0.08$ kHz from the value obtained by the previous analysis. This discrepancy, although exceeding the standard error interval of the fits, is still small enough to be attributed to the scatter of the read-out direction, which limits the reliability of the amplitude extraction from the fringes.

In this section we experimentally showed that the time evolution in a constant magnetic offset field induces a spinor phase evolution which transforms spin length in the transversal plane to alignment. Here, the fully aligned state, i.e. a zero spin length state with fluctuations confined to a plane, is the polar state titled by 45°

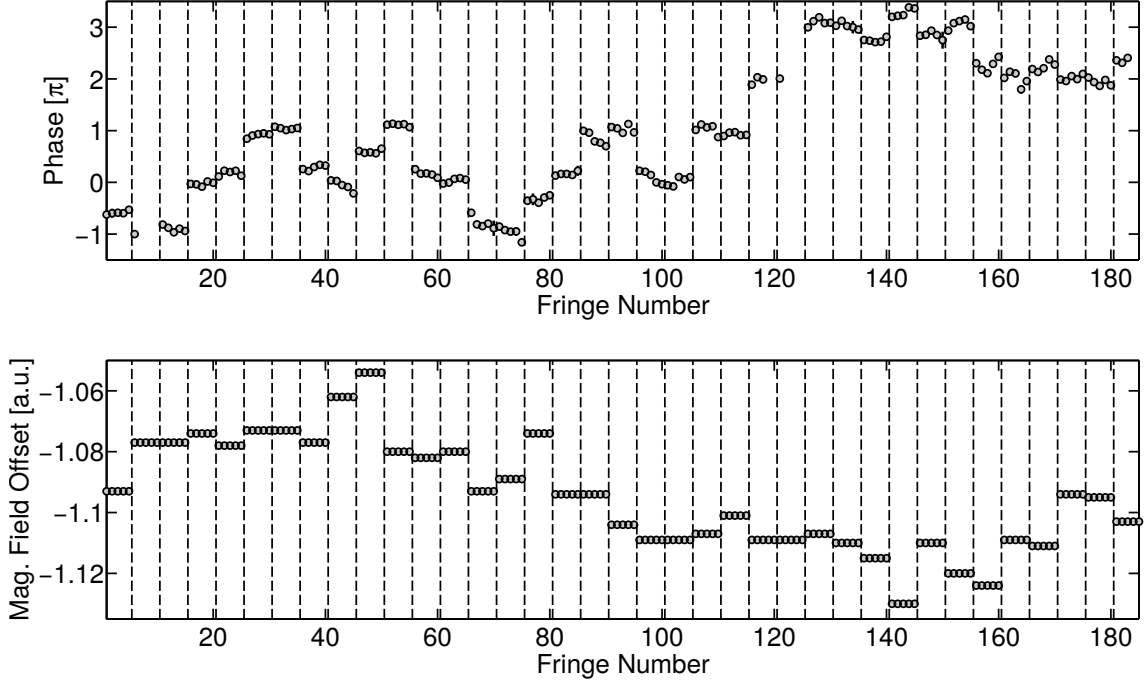


Figure 4.6: After preparing a polar state which is tilted by different angles against the transversal plane the spinor phase of the state is evolved by π to transform the initial alignment to spin length. The upper plot shows the fringe phase from a sinusoidal fit (vertical dashes resemble the fit uncertainty) to 12 spin projections measured by rotating read-out directions in the transversal plane (see fig. 4.7 for exemplary fits). The y -axis (shared with the lower plot) shows the chronological number of the fringe; the whole plot corresponding to a total measurement time of about 1 d. Missing data points correspond to fringes where too many single realisations were discarded to allow reliable fitting. Here, single shots are filtered out due to malfunctions in the experimental control or large atom number fluctuations. The positions of phase steps correspond to points where the magnetic field offset was adjusted to counteract drifts. A value proportional to the current offset on the magnetic field coils is shown in the lower plot. At each vertical dashed line the magnetic field strength was measured and, if required, adjusted via the current offset.

against the transversal plane. By analysing the oscillation frequency a deviation from the magnetically induced second-order Zeeman shift becomes apparent. This difference may be attributed to mean-field shifts which depend on the total density as well as the momentary spin state.

4.2 Preparation and Control of Spinwaves

Spin Wave in the Orientation of the Fluctuations

Next, we want to apply the concept of the spinor phase evolution in external magnetic fields to understand controlling initial spin states. More precisely, here a spin wave is considered. Here, contrary to a spatially oscillating spin projection in this case the direction of fluctuations is varying over the spatial extent of the system. To implement this scenario we initially start from a polar state with vanishing spin length and dipole fluctuations only in the transversal plane. Thus, a direction can be defined by its normal vector, which, in the following, we will call fluctuation or alignment direction.

The experiment is conducted with $\sim 67\,000$ atoms in the elongated waveguide trap. First, all atoms are transferred to the $m_F = 0$ mode by two MW transfers (see fig. 4.8a for the whole preparation scheme) to initialise the polar state. Next, a partial Ramsey sequence is implemented by two RF $\pi/10$ -pulses on a fraction of the total population. Defining the initial rotation axis as F_y , the first pulse tilts the polar state against the transversal plane. This transfers a small fraction of the zero mode population to the side modes. In the external magnetic field these two $m_F = \pm 1$ levels then accumulate a Larmor phase. This corresponds to the precession of the fluctuation direction around the magnetic field axis \mathbf{B} . To generate a spatially dependent phase shift, the magnetic offset field is superimposed with a small spatial gradient field pointing along the longitudinal trap direction. In a frame co-rotating with the Larmor precession induced by the constant offset field this leads to a linear accumulation of Larmor phase with position x along the atomic cloud. Consequently, this results in a precession of the fluctuation direction in space. Additional to the Larmor phase accumulation the side modes also experience a spinor phase evolution while being held in the magnetic offset field. Since the strength of this offset field is much larger than the amplitude of the gradient field, the spinor phase can be assumed to be constant over the extent of the trap. As we have seen in the previous sections 3.3.1 and 4.1, applying this phase evolution to a tilted polar state induces an oscillation in the transversal spin length. Thus, we expect to not only obtain a spin wave in the fluctuation direction but also in the transversal orientation of the spin-dipole components. Thus, the second RF $\pi/10$ -pulse also tilts the transversal spin away from the plane, resulting in a reduction of the perpendicular amplitude by the fraction $1 - \cos(\pi/10) \approx 0.05$.

Because the Hamiltonians of the linear and second-order Zeeman shifts commute the processes of Larmor phase accumulation in the gradient field and spinor phase evolution in the offset field can be treated separately. Here, we first discuss the

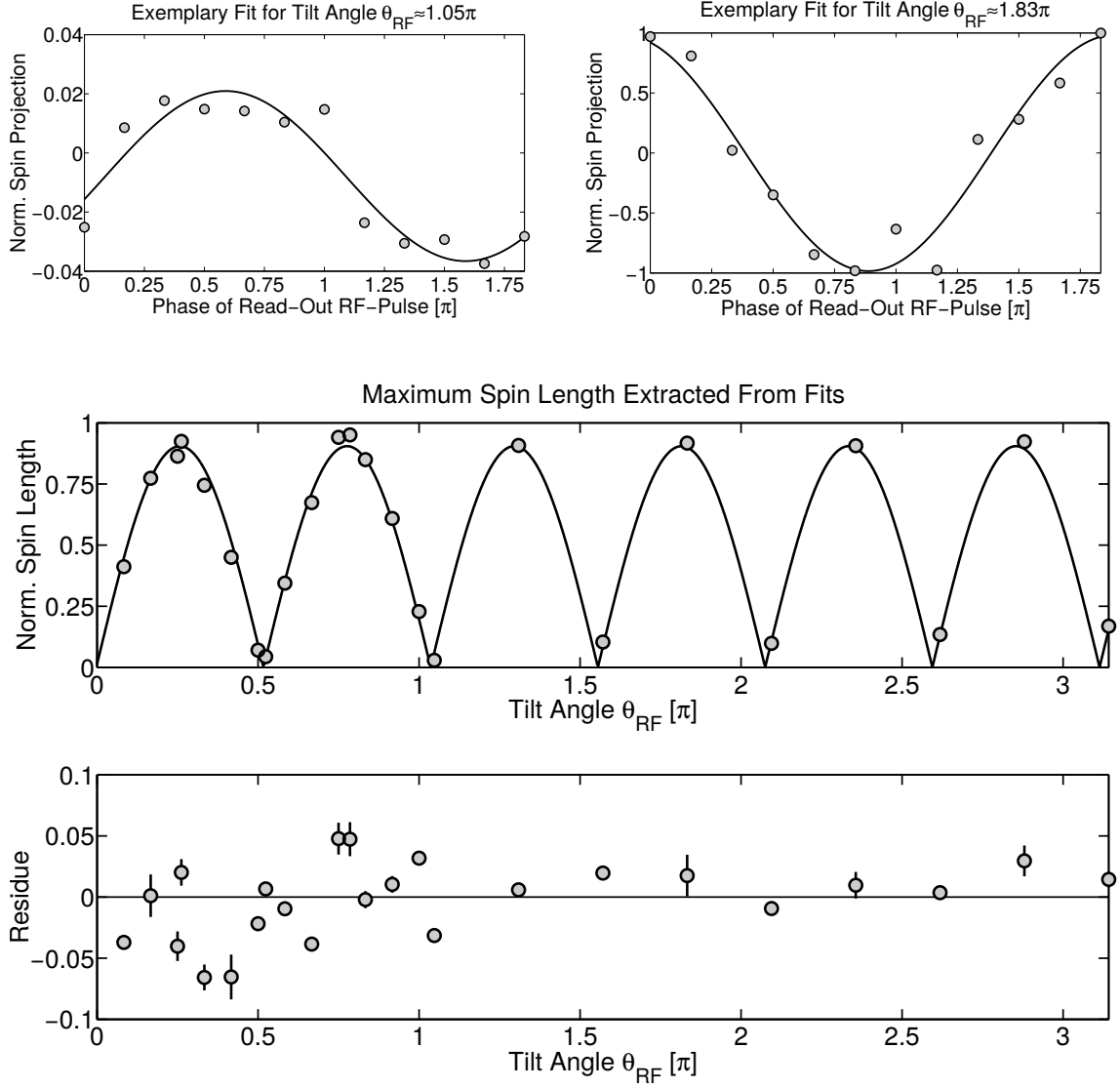


Figure 4.7: A polar state is tilted by angles θ_{RF} against the transversal plane and subsequently a spinor phase evolution of π transforms the initial alignment to spin length. By sampling 12 equally spaced RF-phases for the read-out mapping of the transversal spin projections to the z -axis different directions are extracted (see fig. 4.3 and the corresponding discussion). In the upper panels two exemplary sinusoidal fits to fringes obtained from sampling the polar angle of the projection direction in the transversal plane are shown. The spin amplitudes extracted by this method are used as estimator for the spin length and are plotted against the initial rotation angle θ_{RF} in the central panel. The solid line displayed here is the best fit of eq. (4.3) to the data. Corresponding residues are shown in the lower panel. The vertical lines mark the 1σ error interval of the spin length plotted in the central panel. Its size is extracted from the standard deviation of the mean value across a set of equal fringe measurements.

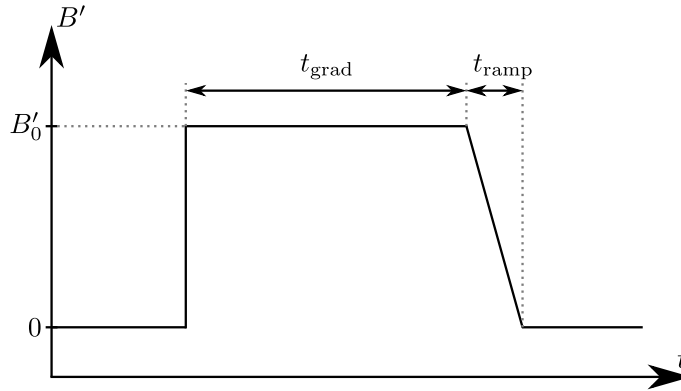
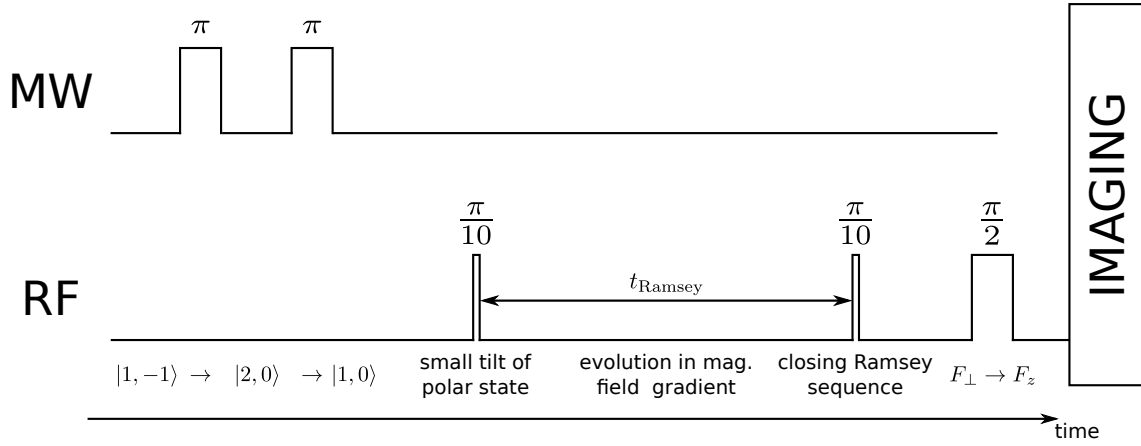
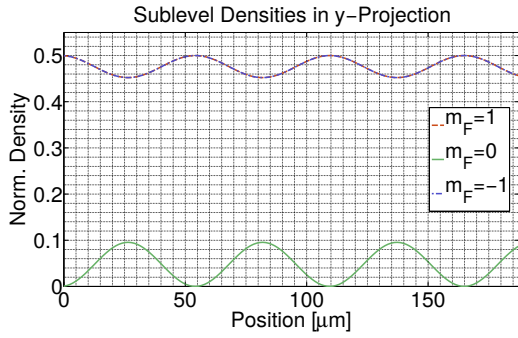
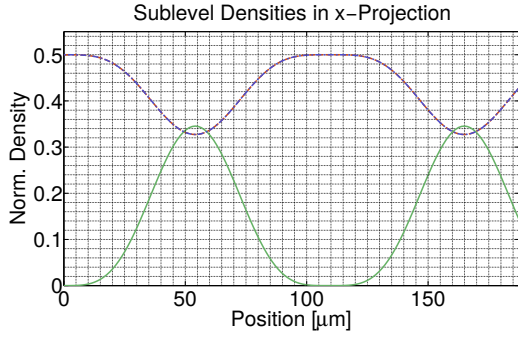


Figure 4.8: Pulse sequence of RF and MW couplings used to generate a spinwave consisting of a polar state with spatially varying tilt axis against the transversal plane (top). To create this spatial variation a Ramsey sequence with $\pi/10$ instead of $\pi/4$ -pulses is used. Here, during the Ramsey interrogation time $t_{\text{Ramsey}} = 100$ ms a spatial magnetic field gradient of B'_0 is applied in longitudinal trap direction (bottom), inducing a linearly increasing accumulation of Larmor phase along the trap. After closing the sequence with the second RF-pulse this phase results in a spatially oscillating tilt angle of the initially state. Additionally, due to a spinor phase evolution during the Ramsey interrogation time a fraction of the spin alignment of the tilted polar state is transformed to spin length (see discussion in the text).

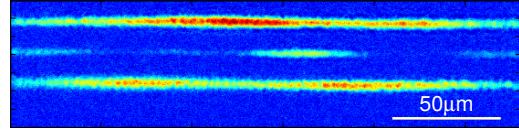
spatial Larmor precession of the fluctuation direction in a frame co-rotating with the constant offset field. This process can easily be evaluated numerically. Here, all RF-pulses are chosen to rotate around F_y . Corresponding results are displayed by fig. 4.9a in form of atomic density profiles. These show the densities expected after mapping the transversal spin-dipole directions F_x and F_y to the z -axis. Both cases show oscillating densities in all modes, corresponding to the precessing fluctuation direction. During the accumulation of Larmor phase this direction is aligned to \mathbf{B} . However, by completing the Ramsey sequence with the second RF $\pi/10$ -pulse the precession axis is tilted around the y -direction. Consequently, the projection of the largest tilt angle appears in the read-out of F_x . Here, the signature of a large tilt is an increased density in the zero mode. Due to the normalisation the oscillation takes place with the same phase in all m_F -levels and because RF-rotations act symmetrically on the side modes there are no density differences between $m_F = \pm 1$, thus $F_z = 0$. Resolving the read-out mapping from the perpendicular plane (i.e. rotating the F_z projection value back to F_x or F_y) this means that the transversal spin projection F_\perp is zero over the whole cloud. This is consistent with the vanishing spin expectation values F_x , F_y , and F_z of the initial state because only length-preserving spin-dipole rotations were executed.

However, comparing this calculation with measured data (fig. 4.9b) shows significant differences: the oscillations in the $m_F = \pm 1$ levels do not occur with the same phase and indicate a non-vanishing spin length. As discussed already, this build-up of transversal spin length originates from the spinor phase evolution during the Ramsey interrogation time. Due to the Larmor phase accumulation in the magnetic gradient field this spin rotates around the z -axis in space. Correspondingly, fig. 4.9c shows the spatial modulation of transversal spin length along the trap for a single realisation. There, the population of the side modes by the first RF-pulse enables the growth of a spin dipole expectation value along the initial rotation axis. Due to the magnetic field gradient applied during that period also the spin dipole component picks up the same spatial modulation in the Larmor phase. Consequently, the spin projection along a transversal direction shows an oscillation at an amplitude corresponding to its length. However, due to the second RF-pulse the amplitude extracted here is reduced by about 5% compared to the actual transversal length. Additionally, superimposed to this Larmor evolution there is the constantly accumulating spinor phase which leads to an oscillation of the spin amplitude in time.

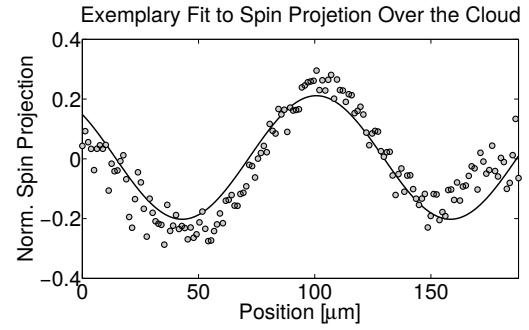
By estimating the expected spin length from the experimental parameters we now want to compare the measurement with the mechanism of spinor phase evolution during the Ramsey interrogation time. Fitting the spatial fringes in the spin projection (see fig. 4.9c for exemplary data) for many realisations allows estimating the spin length of the wave as average over the fit amplitudes: $|F_\perp| = 0.183 \pm 0.004$. Here, the uncertainty corresponds to the error of the mean estimated from the standard deviation across the full set of realisations. This value we now want to compare to the spin length expected from a spinor phase evolution over a period equal to the experimental duration. For simplicity, we neglect the gradient field because it is much smaller than the constant offset field of $B = 0.884$ G (see below for an esti-



(a) Calculated atomic densities for mapping of spin projections F_x and F_y to the z -axis.



(b) Absorption picture of one experimental realization of a spinwave.



(c) Experimentally extracted transversal spin projection with sinusoidal fit.

Figure 4.9: Density profiles and a spin projection for a spinwave in the fluctuation direction of a polar state tilted against the transversal plane. The preparation scheme for the spin wave is given in fig. 4.8. **a)** Calculated spatial density profiles of all m_F -levels for linearly position dependent accumulation of Larmor phase in a system with constant total density. The spinor phase evolution during the Ramsey interrogation time is neglected here. In this case, the tilted polar state accumulates a spatially increasing Larmor phase, leading to an oscillating density distribution along the extent of the system. However, because the densities oscillate with the same phase in all modes this indicates that no transversal spin builds up. The two plots resemble the read-out of the cloud along the F_x (top) and F_y -direction (bottom). **b)** Absorption image of the spinwave with colour-coded atomic densities. From top to bottom the three clouds resemble the $m_F = 1, 0, -1$ components after mapping of a transversal direction to the z -axis with subsequent Stern-Gerlach splitting of the atoms. **c)** Exemplary spin profile extracted from the transversal spin projection (points) along the longitudinal trap axis. The solid line shows the best fit of sinusoidal function which is used to extract the amplitude of the transversal spin.

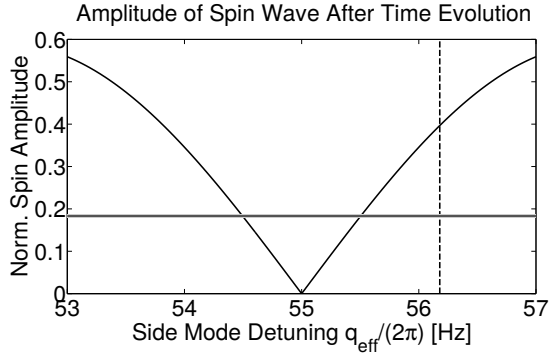
mation of the gradient field magnitude). As evolution time we need to consider the duration $t_{\text{Ramsey}} = 100$ ms between the Ramsey pulses. The RF-pulse mapping of the transversal spin projection to the z -axis directly follows the second $\pi/10$ pulse, thus no evolution after the Ramsey sequence takes place. Also the RF-pulse durations $\tau_{\pi/2}^{\text{RF}} = 14.3 \mu\text{s}$ are much smaller than t_{Ramsey} and can be discarded in the analysis of the spinor phase. Both the first Ramsey pulse and the read-out are assumed to rotate around and project onto the F_x -direction, respectively. Then, by neglecting the tilt of the dipole expectation vector induced by the second Ramsey pulse this procedure corresponds to the spin manipulation presented in section 3.3.1. As mentioned before, this approximation leads to a $\sim 5\%$ overestimation of the actual transversal spin length. An expression for the spin projection was derived previously which describes the transversal spin length

$$|F_{\perp}| = \left| \sin(2\theta) \sin\left(\frac{\varphi_S}{2}\right) \right| \quad (4.4)$$

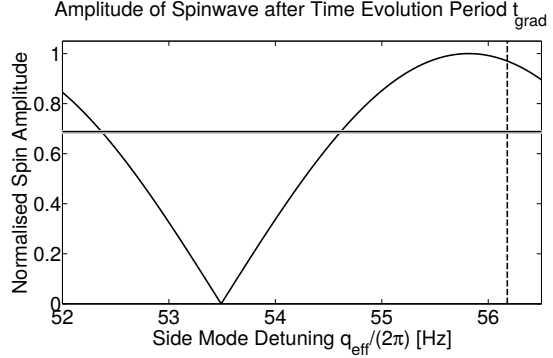
for this example, where $\theta = \pi/10$ is the initial tilt angle of the polar state and the spinor phase $\varphi_S = 2qt_{\text{Ramsey}}$ is accumulated during the Ramsey interrogation period. By keeping the time t_{Ramsey} fixed, fig. 4.10 shows the spin length variation as function of the side mode detuning q_{eff} . As we have already seen in section 4.1 the main contribution to this splitting is given by the second-order Zeeman shift q but there the actual frequency was reduced by about 3 Hz compared to this value. Thus, for the spinwave we expect to find an amplitude corresponding to a side mode splitting q_{eff} close to q which matches the experimental value of ca. 0.183. Figure 4.10a shows two possible values $q_{\text{eff}}/(2\pi)$ for this scenario: about 54.5 Hz and 55.5 Hz. Compared to the first experiment presented in section 4.1 here the atom number is higher but the density is lower due to the weaker confinement in the waveguide potential as compared in the crossed dipole trap. Previously, the shift in the side mode detuning was explained by mean-field shifts. Other experiments (not included here) show that to arrive at about the same mean-field shift in the crossed dipole trap as in the waveguide potential at the current experimental conditions the atom number must be reduced to less than $\sim 20\,000$. Thus, here we expect the actual detuning to be smaller than q by about a factor of $\gtrsim 56\,000/20\,000$ than in the previous measurement. This estimation arrives at $q_{\text{eff}} \gtrsim 2\pi \times 55.1$ Hz which is compatible with the value $q_{\text{eff}} \approx 2\pi \times 55.5$ Hz obtained from fig. 4.10a.

From the picture of the spinor phase evolution we understand that the spin length measured in the experiment has the same periodicity as the Larmor phase modulation. Thus, we can further use the frequency obtained from the fits to the spatial spin projection profile (fig. 4.9c) to infer the magnetic field gradient applied during the Ramsey interrogation time. To obtain the accumulated Larmor phase as function of the position x along the cloud we integrate over the ramp of the magnetic gradient field (see fig. 4.8, bottom):

$$\varphi_L(x) = \tilde{p} \int_0^{t_{\text{end}}} dt B'(t)x t = \tilde{p} B'_0 x \left(t_{\text{grad}} + \frac{t_{\text{ramp}}}{2} \right), \quad (4.5)$$



(a) Spin wave in the fluctuation direction from a tilted polar state.



(b) Spin wave from a fully elongated transversal spin.

Figure 4.10: Calculation of the transversal spin amplitude for two spin waves. The estimations are carried out by assuming a spinor phase evolution of an initial state for a fixed time. The result is plotted against different side mode detunings q_{eff} showing a range of frequencies below the second-order Zeeman shift $q \approx 2\pi \times 56.2$ Hz (dashed vertical line). For each scenario the measured spin amplitude is displayed as horizontal line. **a)** Calculation for a spin wave prepared from a polar state tilted by an angle $\pi/10$ against the transversal plane. The spin amplitude resulting after the spinor phase evolution period of $t_{\text{Ramsey}} = 100$ ms is reduced by ca. 5% to account for the second RF-pulse in the preparation scheme (see text and fig. 4.8). **b)** Spin length for spinor phase evolution for $t_{\text{grad}} = 107.50$ ms of a fully elongated transversal spin. For the preparation scheme of the corresponding measurement, see fig. 4.11.

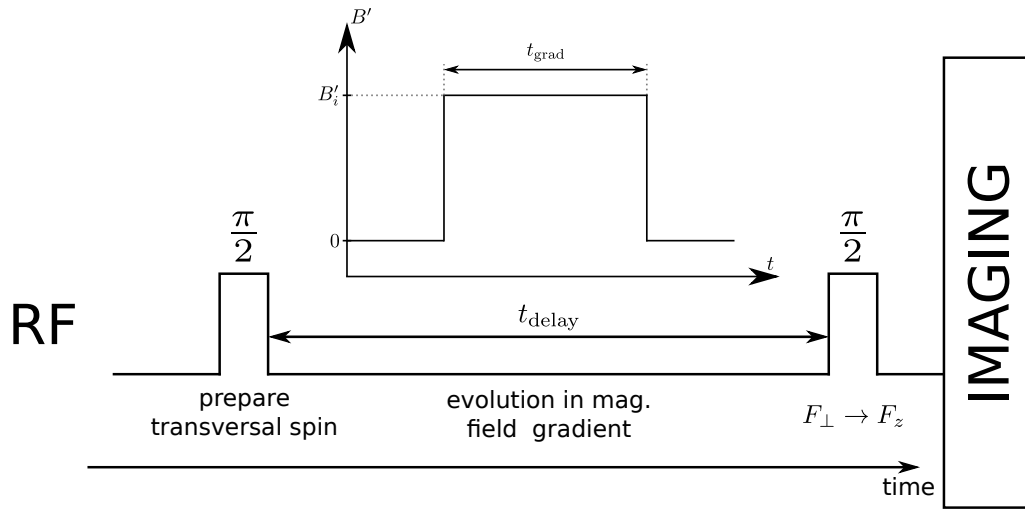
where $\tilde{p} = p/B$ is the linear Zeeman shift per magnetic field strength. Inserting the experimental parameters $t_{\text{grad}} = 80$ ms and $t_{\text{ramp}} = 10$ ms the accumulated phase difference over the cloud $\varphi_{\text{L}}(\ell) - \varphi_{\text{L}}(0) = k\ell$ can be equated with the wave number of the spin wave $k = 2\pi \times (9.1 \pm 0.2) \text{ mm}^{-1}$ estimated from the fits to experimental data. From this we obtain an estimation of the magnetic field gradient applied for the preparation of this spin wave: $B'_0 = (96 \pm 2) \mu\text{G}/100 \mu\text{m}$.

Spin Wave in the Transversal Spin-Dipole Orientation

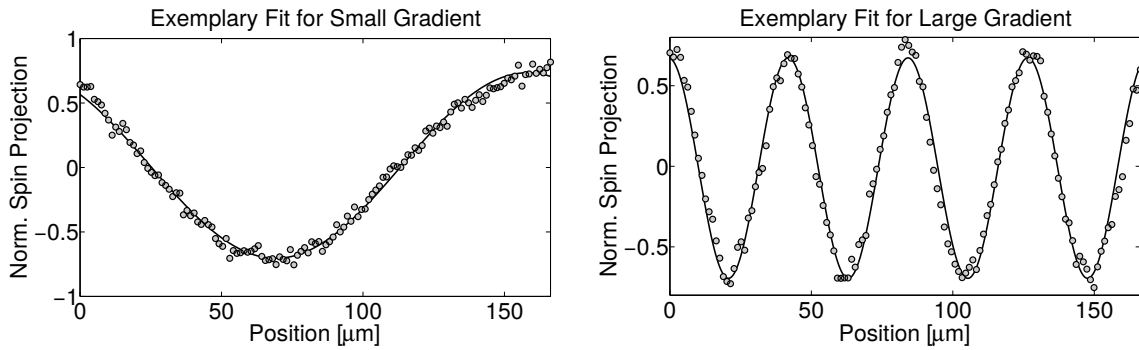
In another experiment a spin wave is prepared from $\sim 36\,000$ atoms in the waveguide potential by first generating a fully elongated spin in the transversal plane by rotating the initial z -spin using a RF $\pi/2$ -pulse. As before, subsequent evolution in a magnetic gradient field induces a spatially varying accumulation of Larmor phase across the trap. Finally, utilising a mapping of the perpendicular spin to the z -basis a projection of the transversal spin is imaged. In this measurement the time delay $t_{\text{delay}} = 107.50$ ms between the two RF-pulses is chosen such that it is a multiple of spinor phase evolution periods: $qt_{\text{delay}} \approx 6$. Applying two gradient fields of different amplitudes $B'_1 = (52 \pm 2) \mu\text{G}/100 \mu\text{m}$ and $B'_2 = (215.4 \pm 0.9) \mu\text{G}/100 \mu\text{m}$ results in two waves of correspondingly different wavelength (see fig. 4.11b for exemplary plots of the spatial variation of a transversal spin projection for both cases). These values are extracted from the data by using similar evaluation methods as above. From the time profile of the magnetic gradient field (see fig. 4.11a) we obtain the spatial dependence of the Larmor phase $\varphi_{\text{L}}(x) = \tilde{p}B'_i x t_{\text{grad}}$ analogously to eq. (4.5). By inserting $t_{\text{grad}} = 100$ ms the field gradients are obtained from the wavenumbers k_i extracted by the fits to the spin projection profiles.

Independent from the spatial frequency, the normalised amplitudes of the spin waves, because the spinor phase evolution only depends on the constant offset field, are both equal within the estimated errors: $|F_{\perp,1}| = 0.69 \pm 0.01$ and $|F_{\perp,2}| = 0.690 \pm 0.006$. However, although the evolution period was chosen to minimise the influence of the spinor phase evolution by accumulating an integer multiple of 2π the spin wave amplitudes extracted in the measurement deviate significantly from the full length of $|F_{\perp}| = 1$. Once more, this confirms the observation from section 4.1 and the evaluation of the previous fluctuation direction wave that the spinor evolution frequency is less than q . Plotting the expected spin length oscillation for the current experiment against the side mode splitting q_{eff} in fig. 4.10b shows two values smaller than q that are compatible with the spin length measurements. Since the relative density distribution between the sublevels (fully elongated transversal spin) is identical with the first measurement in section 4.1 the estimation of the mean-field shifts expected for this system are similar to that case. However, since the other experiment was carried out with larger atom numbers trapped in a much stronger confinement (crossed dipole trap), here the shifts are expected to be smaller than before. Thus, $q_{\text{eff}} \approx 2\pi \times 54.3 \text{ Hz}$ is the most plausible estimation of the side mode detuning for this experiment.

Summarising, we have seen that by utilising small transversal magnetic field gradi-



(a) Preparation sequence of the spin wave.



(b) Exemplary spin projection profiles for different magnetic field gradients.

Figure 4.11: **a)** RF-pulse sequence for generation of Larmor-phase modulated spin wave of a transversal spin. After tilting the initially fully elongated spin to the transverse plane a spatial magnetic gradient field is applied for the duration $t_{\text{grad}} = 100$ ms to induce a spatially varying Larmor phase in the frame co-rotating to the offset field. Afterwards the atoms are imaged by mapping the transversal spin to the quantisation axis with subsequent Stern-Gerlach read-out. **b)** Exemplary sinusoidal fit to two Larmor-phase modulated spin waves generated in two gradient fields of different magnitude.

ents spin waves with different wavelengths and amplitudes can be generated. These parameters are induced by a position-dependent accumulation of Larmor phase and an approximately spatially homogeneous spinor phase evolution. Not only for waves starting from an elongated transverse spin but also for tilted polar states both mechanisms are important. To calibrate the spin amplitude an additional delay period can be inserted between executing the initial RF-rotation and the application of the field gradient to adjust the total amount of accumulated spinor phase. The exact value for this delay, although in first approximation it can be estimated from the second-order Zeeman shift, has to be determined experimentally. The reason for the additional shift seems to originate from mean-field shifts which depend on the total density and the spin state which is being prepared.

4.3 Spin Dipole and Quadrupole Observables in Long-Time Dynamics

Changing the focus from the preparation of spin states to the read-out of operators, here measurements are presented that access different quadrupole observables. For these experiments we are not interested in the evolution on timescales shorter than the inter-particle dynamics. Instead, the evolution periods accessed in these measurements lie one order of magnitude above this scale. In particular, here the evolution following a quench in the side-mode detuning is of interest.

4.3.1 Mean-Field Theory

To understand the changes induced by quenching the side-mode detuning we want to extend the discussion of the Hamiltonian introduced in section 2.2 to the ground states for different experimental parameters. For this, first the field operators are expanded into spatial modes (see eq. (2.14)). Then, assuming the atomic cloud forms a condensate in the spatial mode with wavenumber $k = 0$, for the corresponding Fock operators the Bogoliubov approximation is applied. This allows replacing all zero momentum modes by their corresponding $k = 0$ mean-field wave functions. Finally, to diagonalise the resulting Hamiltonian the Bogoliubov transformation is applied to rotate the spatial modes to the eigensystem. For a more detailed discussion of this treatment, see [4, 19, 13].

From the eigenenergies the calculation of the groundstates for the side mode detuning q is possible. Note here that the spin-spin coupling constant c_1 of the ^{87}Rb $F = 1$ hyperfine manifold is negative, thus inducing ferromagnetic interaction. For the following experiments two ground state phases are of interest: the polar phase and the symmetry-broken easy plane ferromagnetic phase. In the former,

constrained by $q > 2n|c_1|$, the ground state is the polar state

$$\Psi = \begin{pmatrix} 0 \\ 1 \\ 0 \end{pmatrix}, \quad (4.6)$$

which, as we have already seen, has no spin length and only fluctuations in the transversal plane. Here, in the limit of large zero-mode population the dispersion relation

$$\omega_k = \sqrt{(\epsilon_k + q)(\epsilon_k + q + 2nc_1)} \quad (4.7)$$

of the side modes can be derived. Proceeding to lower values $0 < q < 2n|c_1|$, we arrive at the easy-plane ferromagnetic phase where the ground state is given by

$$\Psi = \frac{1}{2} \begin{pmatrix} \sqrt{1 - \tilde{q}} \\ \sqrt{2(1 - \tilde{q})} \\ \sqrt{1 - \tilde{q}} \end{pmatrix}. \quad (4.8)$$

It has a q -dependent spin length $|F_\perp| = \sqrt{1 - \tilde{q}^2}$ confined to the transversal plane, where $\tilde{q} = -q/(2n|c_1|)$. [4]

4.3.2 Spin-Changing Collision Dynamics

At the magnetic offset fields of $B \approx 1.44$ G the second-order Zeeman shift introduces a side-mode detuning $q > 2n|c_1|$, which means that the mean-field ground state of the system lies in the polar phase. Consequently, after preparing a polar state $|\Psi\rangle = (0, 1, 0)$ no dynamics takes place. However, when the side mode detuning q_{eff} is suddenly changed to a value in the interval $(0, 2n|c_1|)$ (easy-plane ferromagnetic phase), the corresponding mean-field ground state changes as well (see section 4.3.1). This already suggests that due to quench-induced modification of the energy spectrum (4.7) the polar state will not remain stationary any more. In fact, this equation shows that for q_{eff} in this phase unstable modes exist. These solutions of eq. (4.7) possess complex energies which induce an exponential growth of their population during time evolution. Since they arise from the spin-changing collision (SCC) term $\hat{\Psi}_0^\dagger \hat{\Psi}_0^\dagger \hat{\Psi}_1 \hat{\Psi}_{-1} + h.c.$ in the interaction Hamiltonian (2.12), tuned into resonance by the adjustment of q_{eff} , their effect is a redistribution of population from $m_F = 0$ to $m_F = \pm 1$. Although the Bogoliubov approximation is strictly applicable only for vanishing side mode occupation, experiments show that this redistribution drives the system to large side mode population on the order of the total atom number. This process generates transversal spin excitations at and below the most unstable Bogoliubov momentum k . This growth takes place on timescales of ~ 300 ms while in the following 3 s a redistribution of the excitations at small spatial frequencies follows. This situation of transversal spin excitations at an approximately constant spin length is compatible with the mean-field ground state

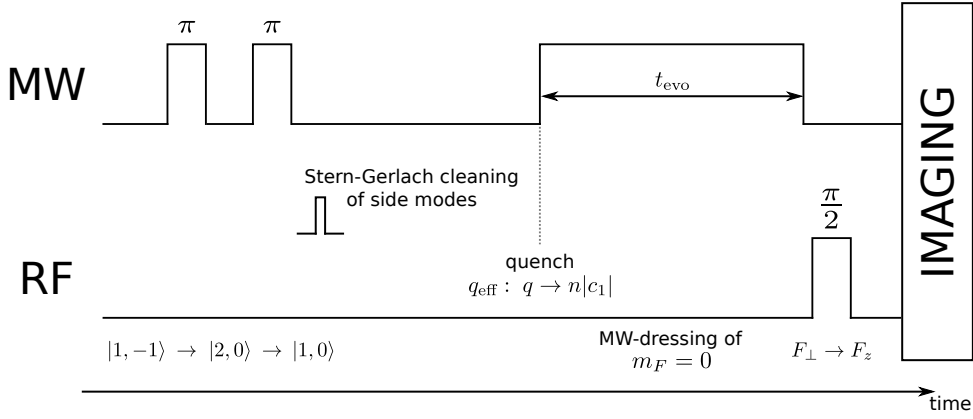
(4.8) of the symmetry-broken easy-plane ferromagnetic phase, which is degenerate for all transversal directions.

Although this state should correspond to the stationary ground state, with increasing evolution time the spin length slowly decreases. This observation, although not captured by the microscopic mean-field theory outlined in section 4.3.1, may be explained by a redistribution of spin-dipole populations to quadrupole excitations. To investigate this, in the following measurements not only spin dipole operators but also quadrupole observables are extracted.

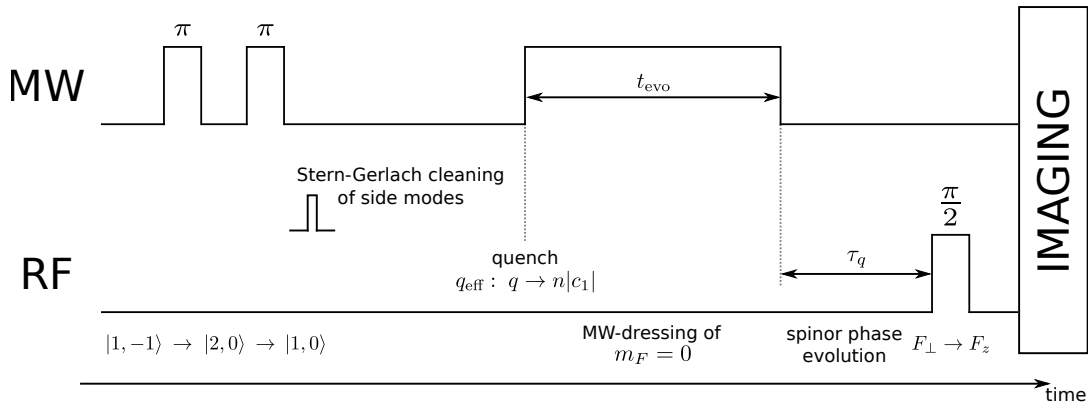
4.3.3 Experimental Setup and Read-out of Observables

For these experiments $\sim 35\,000$ atoms are loaded into the waveguide potential and transferred to the $m_F = 0$ level via MW transfers (see fig. 4.12). Next, any remaining atoms in the side modes are removed by a Stern-Gerlach gradient pulse. To initiate the SCC dynamics, the $m_F = 0$ level is shifted to a larger energy by MW-dressing. Here, the signal generator is set to a frequency blue-detuned by $\delta \approx 2\pi \times 182$ kHz to the transition $|1, 0\rangle \leftrightarrow |2, 0\rangle$ which induces an AC-Zeeman shift $q_{\text{MW}} = \Omega_{\text{MW}}/(4\delta)$ on $|1, 0\rangle$, where $\Omega_{\text{MW}} \approx 2\pi \times 10.11$ kHz is the Rabi frequency of the aforementioned MW-coupling. Suddenly switching on this off-resonant Rabi coupling induces the quench $q_{\text{eff}} = q \rightarrow q_{\text{eff}} = q - q_{\text{MW}}$ which is tuned such that the final value is $q_{\text{eff}} \approx n|c_1|$. Under these conditions the system evolves for the period t_{evo} before extracting the observables. In the following measurements read-out schemes for three different operators are applied: \hat{F}_x , \hat{Q}_{yz} , and \hat{Q}_{xy} . These are carried out as described in the respective subsections of chapter 3. For the read-out of the spin dipole the usual RF-mapping to the z -axis is applied. By evolving the atoms without dressing before the mapping pulse, i.e. evolving the spinor phase by π at large $q_{\text{eff}} = q \approx 2\pi \times 149$ Hz, allows the access of Q_{yz} . Finally, to extract Q_{xy} the side modes are mixed by transferring $|1, 1\rangle \rightarrow |2, 0\rangle$ with subsequent MW $\pi/2$ -coupling to $|1, -1\rangle$. Note however, that the observables \hat{Q}_{yz} and \hat{Q}_{xy} described here are connected to another set of operators \hat{Q}_{xz} and $\hat{Q}_{y^2-x^2}$ via a $\pi/2$ -phase shift in the mapping or mixing pulses (see chapter 3). As we have seen in the previous measurements the phase of the pulses relative to the Larmor phase of the system is scrambled by magnetic field fluctuations. Thus, the quantities accessed here are always projections along a superposition of these operator pairs $(\hat{Q}_{yz}, \hat{Q}_{xz})$ and $(\hat{Q}_{xy}, \hat{Q}_{y^2-x^2})$. Nevertheless, to minimise notational complexity they will be referred to as initially introduced above.

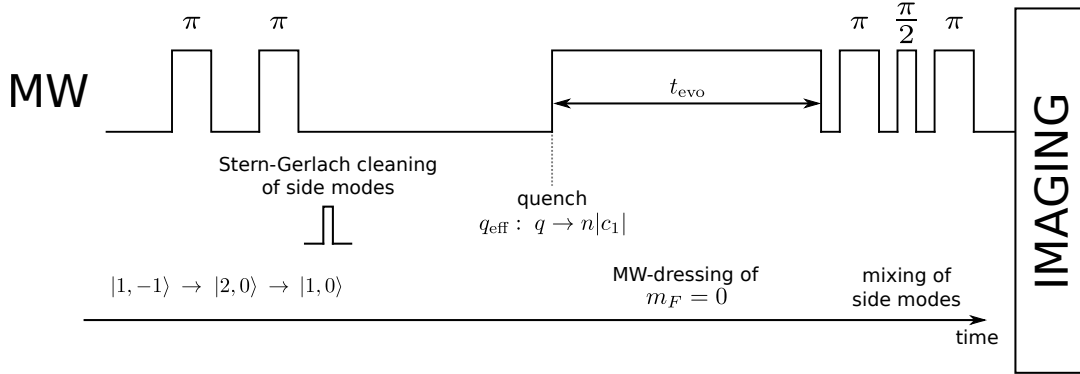
To tune the side-mode offset to $q_{\text{eff}} \approx n|c_1|$ an additional characterisation measurement is carried out. There, for different MW-detunings δ the atoms are held for $t_{\text{evo}} = 4$ s before extracting the population of the side-modes. As function of δ the occupation numbers show a clear resonance with a width of about 4 Hz (see fig. A.2), which should correspond to the range of q_{eff} in the easy-plane ground state phase where unstable Bogoliubov modes around the polar state exist. Due to density-dependent mean-field shifts of the sublevels and off-resonant MW-coupling to the



(a) Read-out of \hat{F}_x



(b) Read-out of \hat{Q}_{yz}



(c) Read-out of \hat{Q}_{xy}

Figure 4.12: Pulse sequences for the readout of different observables after long-time dynamics following a quench in the side-mode detuning to $q_{\text{eff}} \approx n|c_1|$. First, the atoms are prepared in the polar state $|\Psi\rangle = (0, 1, 0)^T$. Then, a quench of the energetic side-mode shift tunes SCCs into resonance, which induces a build-up of transversal spin at the beginning of the evolution period t_{evo} . Afterwards three different observables are extracted: **a)** \hat{F}_x , **b)** \hat{Q}_{yz} with $\tau_q = 2\pi/(2q)$, and **c)** \hat{Q}_{xy} .

other $F = 1$ and $F = 2$ states during the dressing period the actual detuning q_{eff} deviates from the estimation $\sim 2\pi \times 9$ Hz provided above. Thus, the correct setting is estimated by the centre of the resonance feature in the side mode population. Based on this method, all values of q_{eff} given in the following are distances to the left edge (first point with a side mode population much larger than zero) of the corresponding resonance feature for the respective measurements.

4.3.4 Results

F_x and Q_{yz} Read-Out

To analyse the measurements, here the observables are extracted spatially resolved along the longitudinal trap direction. For a central region of ca. $120 \mu\text{m}$, where the total density is approximately constant (see fig. A.1) we extract the quantities detailed below. Across all experimental realisations with equal parameters histograms are built up from locally measured values for each pixel in this central region. Here, we first extract the transversal spin F_x , whose distributions are shown in fig. 4.13, for a quench to $q_{\text{eff}} \approx 2\pi \times 1.5$ Hz (see fig. A.2 for the SCC resonance feature). Initially, the histogram resembles a narrow Gaussian centred around zero as is anticipated for the polar state. Then, the distribution quickly broadens (0.5 s) and develops a double-peaked structure (2 s). This feature is present until the last evolution time of 8 s accessed in the measurement, while the maxima of the peaks slowly move towards the middle. This double-peaked feature is compatible with the distribution expected from spin projections along a fixed direction of a randomly oriented transversal spin with approximately fixed length. To extract the mean amplitude $\langle F_x \rangle$ of this spin and its fluctuations σ the histograms are fitted by a distribution $p(F_x) \sim 1/\sqrt{1 - (F_x/\langle F_x \rangle)^2}$ convolved with a Gaussian of standard deviation σ to capture the fluctuations in the spin length. Evaluating the histograms where such a fit was sensible shows that the spin amplitude decreases from an initial value of 0.6 at 2 s over the whole period of evolution times to a final length of 0.4 at 8 s. However, over the whole sample the fluctuations stay approximately constant at $\sigma \approx 0.1$.

To investigate if this reduction in the length might be explained by an evolution of the spinor phase also the alignment of the state is measured. As we have seen in section 4.1 a fully elongated transversal spin is transformed to a polar state tilted by 45° against the transversal plane. This state resembles a \hat{Q}_{xz} or \hat{Q}_{yz} eigenstate, depending on the initial spin orientation along F_y or F_x , respectively. Consequently, to access the appropriate quadrupole projections we apply the read-out scheme introduced in section 3.3.2 to access Q_{yz} . Figure 4.14 displays the results obtained for this observable after executing the same quench as before. Initially, the histograms show a narrow Gaussian, which again is compatible with the polar state. Similar to the F_x -data also the quadrupole histograms feature a fast broadening within the first second of the evolution. However, here no double-peak structure builds up. Instead, for all times the histograms remain nearly Gaussian around $Q_{yz} = 0$. Thus, no clear excitations of the Q_{yz} -length can be identified. Over time,

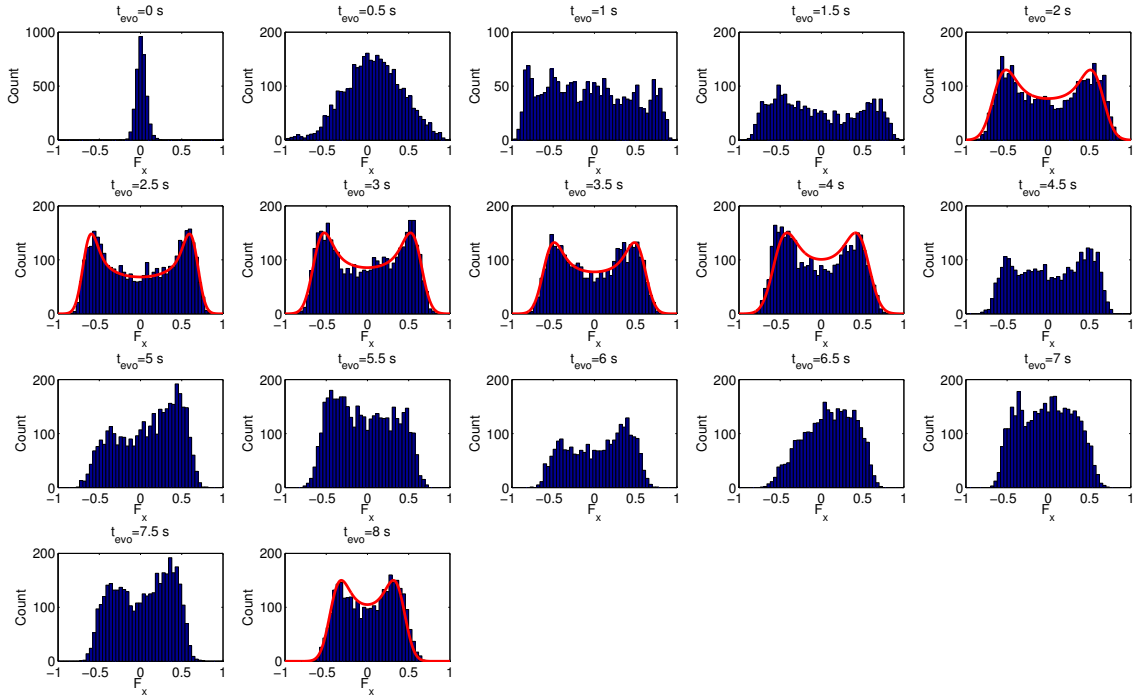


Figure 4.13: Initially, a polar state is prepared. Then, following a quench in the side mode detuning to $q_{\text{eff}} \approx 2\pi \times 1.5$ Hz the atoms are held at this value for a time t_{evo} before the transversal spin (here denoted as F_x) is extracted. The first histogram shows a narrow Gaussian distribution centred around zero spin projection, which resembles the expectation for the polar state. Induced by SCC dynamics within ~ 0.5 s this distribution quickly broadens and afterwards transforms to develop a clear double-peaked structure at 2 s. This qualitative feature stays present in most distributions until the last evolution time $t_{\text{evo}} = 8$ s measured here. Where applicable, this structure is approximated by the probability distribution for measuring a randomly oriented spin projected onto a constant direction (see text). Best fits of this model are displayed as red solid line. The extracted spin amplitude shows a slow reduction while maintaining approximately constant fluctuations in the length over time (see text).

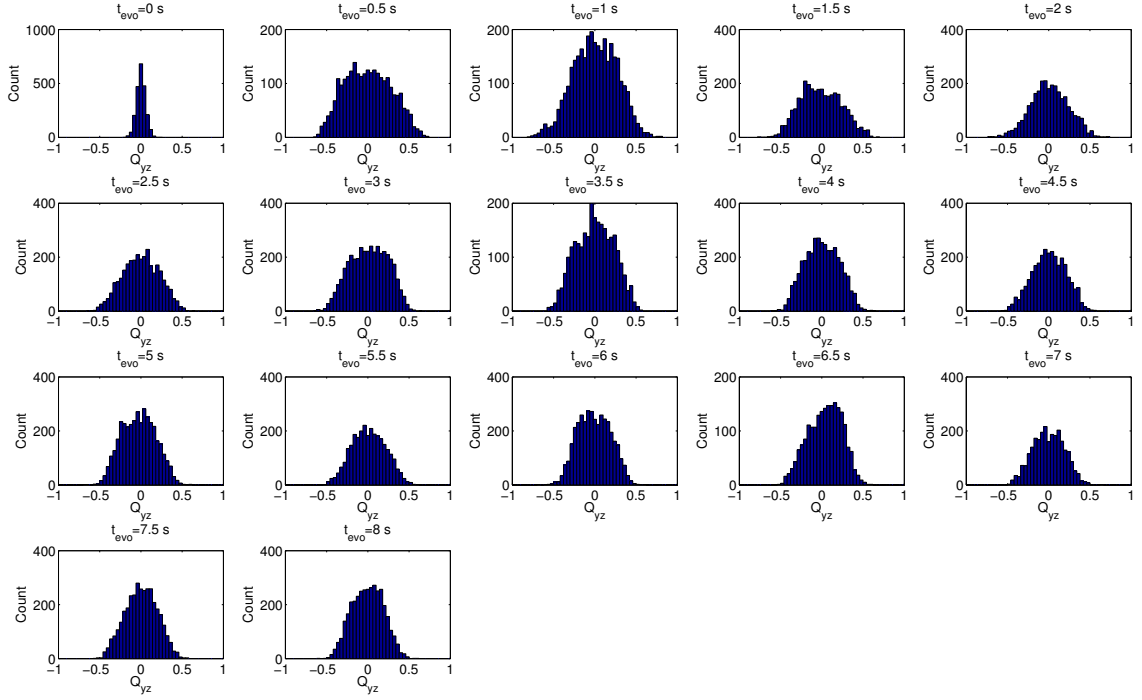


Figure 4.14: After preparation of a polar state the side mode detuning is quenched and the atoms are held at these conditions for an evolution time t_{evo} (equivalent to fig. 4.13). Afterwards, the quadrupole projection Q_{yz} is extracted. As expected for the initial polar state the first distribution resembles a narrow Gaussian centred around zero. Similar to F_x in fig. 4.13 the distribution quickly broadens within 0.5s but no double-peaked structure develops. Instead, for all evolution times the histograms remain approximately Gaussian around zero. Consequently, unlike for F_x no quadrupole length excitations of sufficient size can be extracted from the data.

the standard deviation of the distributions declines from ca. 0.3 at 0.5 s to 0.2 at 8 s. This suggests that the SCCs generate a state of strongly increased fluctuations in this quadrupole. Consequently, because the Q_{yz} -distributions do not show a double-peaked structure, this measurement can exclude a simple spinor phase rotation as reduction process of the transversal spin observed in fig. 4.13.

Q_{xy} Read-Out

For this measurement the experiment is carried out analogously to before but the final side mode detuning after the quench is $q_{\text{eff}} \approx 2\pi \times 2.5 \text{ Hz}$ (see fig. A.3 for the SCC resonance). Instead of analysing the Q_{yz} quadrupoles, here F_x and Q_{xy} are extracted from the data. In fig. 4.15 the F_x -distributions show a similar build-up of the double-peaked structure as observed before in fig. 4.13. Also the initial and final positions of the double-peak maxima show no significant change to before. Similar to Q_{yz} from before also Q_{xy} (fig. 4.16) shows an initially localised Gaussian around $Q_{xz} = 0$ like expected for the polar state. Next, the histograms quickly broaden after the quench while maintaining their single-peaked structure centred at zero. Although the shape of the distribution at 2.5 s may suggest two peaks close to the centre they are not pronounced enough to unambiguously be identified as such across all times. Further, also here the standard deviation of the Q_{xy} -distribution reduces from about 0.3 at 0.5 s to ca. 0.2 at 8 s. This leads to a similar conclusion as above: while the SCC dynamics largely enhances the quadrupole fluctuations no clear length-excitations of sufficient size can be identified.

Concluding, these measurements show that dynamics following the quench affects the quadrupoles mainly in the size of their fluctuations. Furthermore, a transfer of excitations from the transversal spin to Q_{yz} or Q_{xy} which may explain the reduction of the spin length over time is not clearly observed. However, the simultaneous decrease of the transversal spin and fluctuations of the quadrupoles suggests a common mechanism driving this evolution.

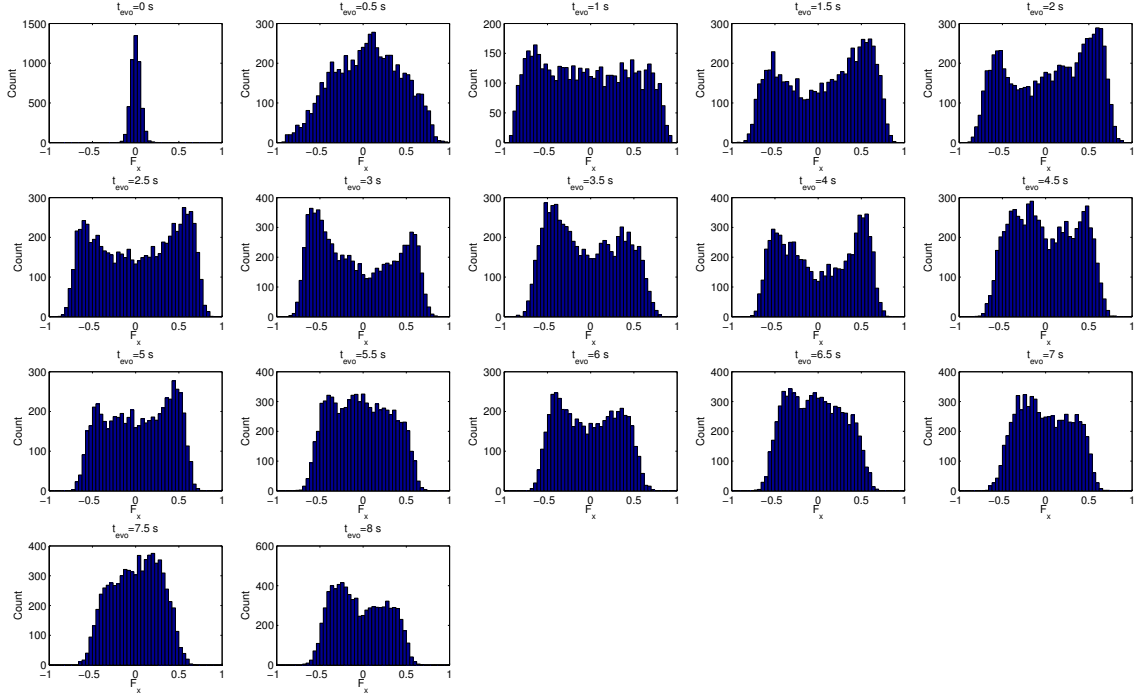


Figure 4.15: Initially, a polar state is prepared. Then, following a quench in the side mode detuning to $q_{\text{eff}} \approx 2\pi \times 2.5$ Hz the atoms are held at this value for a time t_{evo} before the transversal spin (here denoted as F_x) is extracted. Analogous to fig. 4.13, from an initially narrow Gaussian centred around zero a broad distribution with double-peaked structure builds up.

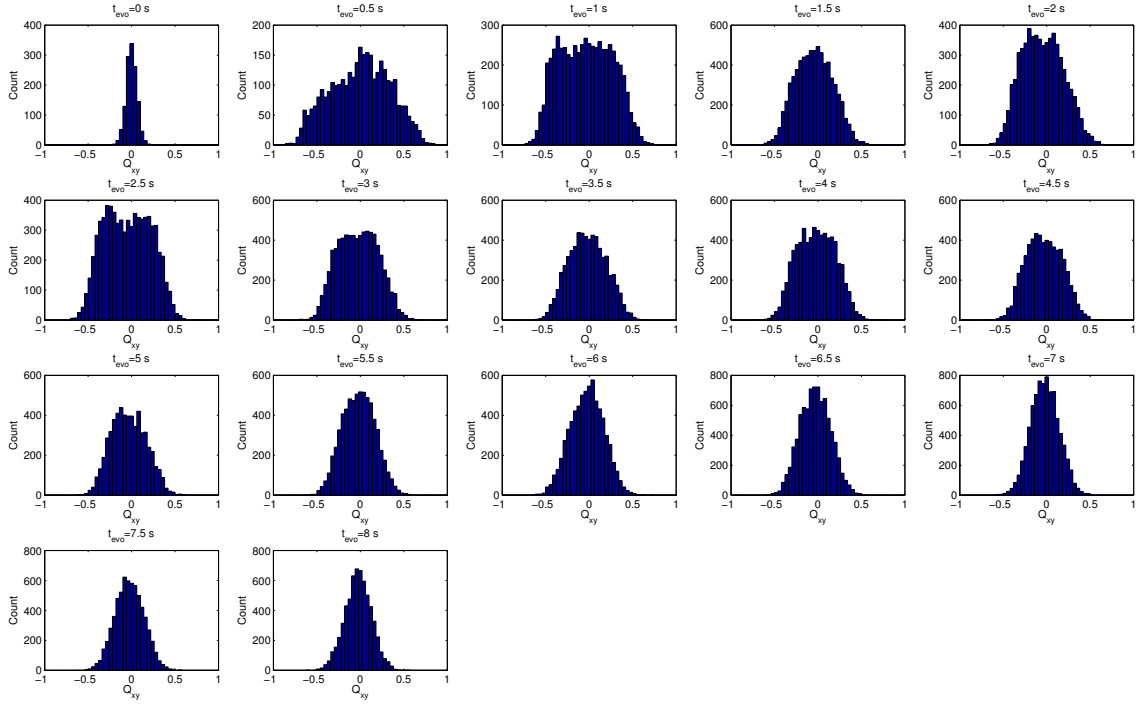


Figure 4.16: Equivalently to fig. 4.15, initially a polar state is prepared, the side mode detuning is quenched, and the atoms are held for an evolution time of t_{evo} under these conditions. Subsequently, the quadrupole projection Q_{xy} is extracted. Similar to fig. 4.14 the initial Gaussian distribution of the polar state quickly broadens and stays approximately single-peaked around zero over time. Although for $t_{\text{evo}} = 2.5$ s a slightly double-peaked structure can be identified on top of the broad distribution, in general no clear length excitations can be extracted from the data.

5 Conclusion and Outlook

This work presents methods to experimentally control the degrees of freedom of a spin-1 system. On the one hand the populations of the magnetic sublevels can be controlled by RF- and MW-pulses, on the other changes of the phases are implemented by time evolutions in an external magnetic field. Here, the Larmor and spinor phase are controlled by the linear and second-order Zeeman shift, respectively. Using these techniques, spinor phase rotations can be implemented, which transform spin to alignment and vice versa, i.e. the spin length is changed. This method is then applied to generate spin waves with different amplitudes.

Furthermore, by performing rotations of the spin state prior to the measurement the spin-1 dipole and quadrupole projections can be mapped to magnetic sublevel densities for read-out. Subsequently, these are measured by a Stern-Gerlach separation of the different components followed by absorption imaging. To access the quadrupoles, on the one hand a measurement scheme for read-out of the Q_{xz} and Q_{yz} projections via a spinor phase rotation by π and subsequent mapping of the transversal spin projections to F_z is provided. On the other hand, Q_{xy} and $Q_{y^2-x^2}$ can be measured by mixing of the $m_F = \pm 1$ levels with a $\pi/2$ Rabi-pulse followed by a mapping of the spin projections as before. For long-time dynamics these schemes are applied to investigate the theoretically unexpected loss of spin length. Here, the temporal evolution in both the dipole as well as quadrupole observables suggests an overall decay of coherences, which will be subject of further studies.

To expand the measurement capabilities of the current setup, the methods presented here may be combined with shelving techniques similar to the spin-sensitive in-situ imaging described in [11]. MW-pulses can be used to transfer a part of the $F = 1$ population to the $F = 2$ manifold. Here, their phase control allows retaining or manipulating the relative phases of the different magnetic sublevels. By choosing these phases appropriately, in the different hyperfine manifolds a subsequent RF-pulse maps orthogonal spin projections to the z -axis for read-out. Thus, these methods can be extended to allow the extraction of both quadratures simultaneously.

Also the possibility for a spatially selective addressing of spins is shortly elaborated here. As we have seen in chapter 3 MW- and RF-pulses can be applied to globally address the spin states. For extending these to allow for local addressability a steerable focused laser beam is used to select a small region of the trap. By detuning the laser from a transition locally confined AC-Stark shifts of the atomic levels can be implemented. This shift, in turn, allows to select (deselect) the addressed region of the cloud in MW-pulses by setting their frequency to resonance in the addressed (non-addressed) region. Furthermore, local Larmor and spinor phase evolutions can be directly implemented by generating an effective magnetic field at the position

of the focused laser by utilising the vector stark shift. [20] Further, by modulating the laser intensity this allows a spatially confined coupling of the magnetic sublevels analogous to RF-pulses, i.e. the implementation of spin rotations [21]. Thus, these techniques offer the same possibilities for spin manipulations as discussed in this work but with additional local control. In particular, this also allows spatially modulating the projection direction in the read-out procedure.

Further, a different imaging approach may additionally enhance the capabilities of the setup. Here, dispersive birefringent imaging provides a direct spin-dependent atom-light interaction in the imaging process. [22, 11] By accessing the phase shift experienced by light interacting with the atoms the spin projection onto the propagation direction of the probe light may be inferred. Additionally, because this technique does not remove the atoms from the trap it provides a non-destructive imaging tool.

A Additional Plots for Long-Time Dynamics

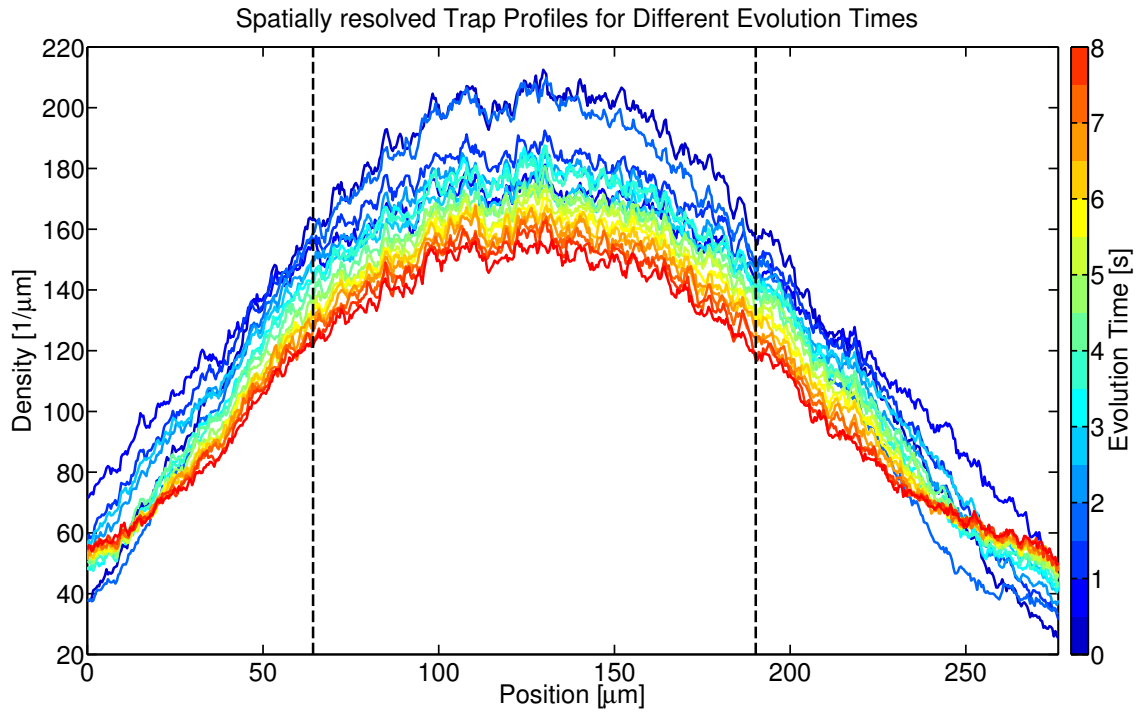


Figure A.1: Initially a polar state is prepared, the side mode detuning is quenched to $q_{\text{eff}} \approx 2\pi \times 1.5$ Hz, and the atoms are held at these conditions for an evolution time up to 8 s. The lines in the plot resemble the total densities in the waveguide potential after the different times. The range between the vertical dashed lines resembles the region evaluated in section 4.3.4.

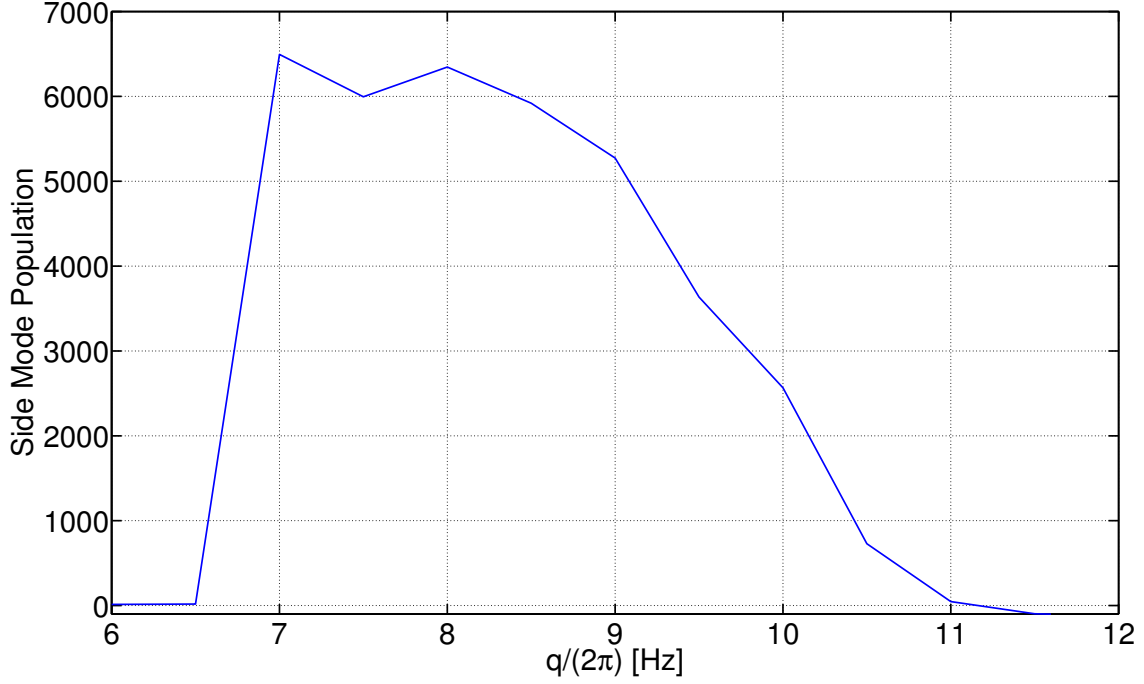


Figure A.2: Spectroscopy signal of the SCC dynamics in section 4.3.4 for the read-out of F_x and Q_{yz} . Initially a polar state is prepared, the side-mode detuning q is quenched to different values, and the side mode population is extracted after an evolution time of 4 s. Here q is calculated as described in section 4.3.3. Due to mean-field shifts and off-resonant coupling between the different $F = 1$ and $F = 2$ levels the values of q shown in the plot deviate from the actual side mode detuning q_{eff} . The resonance feature visible here corresponds approximately to values of q_{eff} between 0 and $2n|c_1|$. In the experiments of section 4.3.4 the final quench value $q = 2\pi \times 8.5$ Hz ($q_{\text{eff}} \approx 2\pi \times 1.5$ Hz) is used.

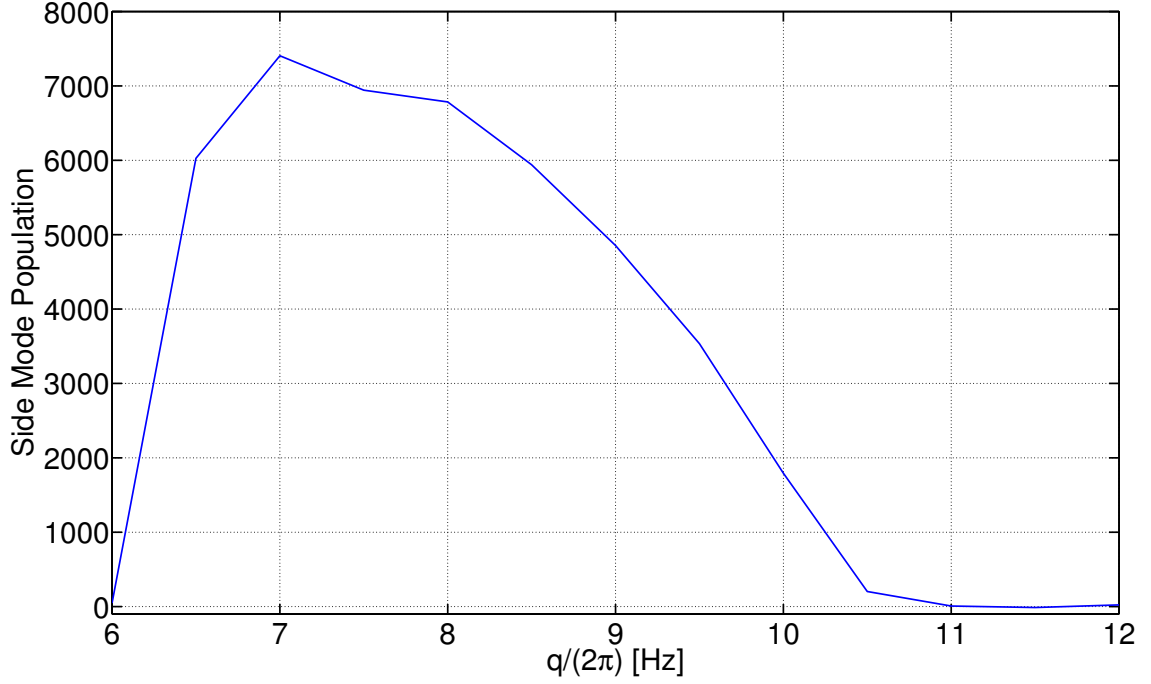


Figure A.3: Spectroscopy signal of the SCC dynamics in section 4.3.4 for the read-out of F_x and Q_{xy} . Initially a polar state is prepared, the side-mode detuning q is quenched to different values, and the side mode population is extracted after an evolution time of 4 s. Here q is calculated as described in section 4.3.3. Due to mean-field shifts and off-resonant coupling between the different $F = 1$ and $F = 2$ levels the values of q shown in the plot deviate from the actual side mode detuning q_{eff} . The resonance feature visible here corresponds approximately to values of q_{eff} between 0 and $2n|c_1|$. In the experiments of section 4.3.4 the final quench value $q = 2\pi \times 9$ Hz ($q_{\text{eff}} \approx 2\pi \times 2.5$ Hz) is used.

Bibliography

- [1] Anatoli Polkovnikov, Krishnendu Sengupta, Alessandro Silva, and Mukund Vengalattore. Colloquium: Nonequilibrium dynamics of closed interacting quantum systems. *Rev. Mod. Phys.*, 83:863–883, Aug 2011.
- [2] Dan M. Stamper-Kurn and Masahito Ueda. Spinor bose gases: Symmetries, magnetism, and quantum dynamics. *Rev. Mod. Phys.*, 85:1191–1244, July 2013.
- [3] C. S. Gerving, T. M. Hoang, B. J. Land, M. Anquez, C. D. Hamley, and M. S. Chapman. Non-equilibrium dynamics of an unstable quantum pendulum explored in a spin-1 bose-einstein condensate. *Nature Communications*, 3, Nov 2012.
- [4] Yuki Kawaguchi and Masahito Ueda. Spinor bose–einstein condensates. *Physics Reports*, 520(5):253 – 381, 2012.
- [5] C. D. Hamley, C. S. Gerving, T. M. Hoang, E. M. Bookjans, and M. S. Chapman. Spin-nematic squeezed vacuum in a quantum gas. *Nature Physics*, 8: 305–308, Feb 2012.
- [6] Walter Geiner and Berndt Müller. *Quantum Mechanics - Symmetries*. Springer-Verlag, second edition, 1994.
- [7] Christopher David Hamley. *Spin-Nematic Squeezing in a Spin-1 Bose-Einstein Condensate*. PhD thesis, Georgia Institute of Technology, 2012.
- [8] Thai M. Hoang. *Quantum Control of a Many-Body System in a Spin-1 Bose-Einstein Condensate*. PhD thesis, Georgia Institute of Technology, 2013.
- [9] H. M. Bharath, M. Boguslawski, M. Barrios, L. Xin, and M. S. Chapman. Singular Loops and their Non-Abelian Geometric Phases in Spin-1 Ultracold Atoms. January 2018, arXiv:1801.00586.
- [10] Daniel Linnemann. *Quantum-Enhanced Sensing Based on Time Reversal of Nonlinear Dynamics*. PhD thesis, University of Heidelberg, 2017.
- [11] G. E. Marti and D. M. Stamper-Kurn. Spinor Bose-Einstein gases. November 2015, arXiv:1511.01575.
- [12] Corey S. Gerving. *Dynamics Of A Quantum Inverted Pendulum Explored In A Spin-1 BEC*. PhD thesis, Georgia Institute of Technology, 2013.

- [13] Lev Pitaevskii and Sandro Stringari. *Bose-Einstein Condensation*. Oxford University Press, 2003.
- [14] Bernd Eiermann. *Kohärente nichtlineare Materiewellendynamik - Helle atomare Solitonen*. PhD thesis, Universität Konstanz, 2004.
- [15] Daniel A. Steck. Rubidium 87 D Line Data. 2003.
- [16] Wolfgang Muessel. *Scalable Spin Squeezing for Quantum-Enhanced Magnetometry with Bose-Einstein Condensates*. PhD thesis, Universität Heidelberg, 2014.
- [17] Paola Cappellaro. Quantum Theory of radiation interactions, fall 2012. accessed: 12/03/2018.
- [18] Fabrice Gerbier, Artur Widera, Simon Fölling, Olaf Mandel, and Immanuel Bloch. Resonant control of spin dynamics in ultracold quantum gases by microwave dressing. *Phys. Rev. A*, 73:041602, Apr 2006.
- [19] Maximilian Prüfer. Structure Formation in a Quenched Antiferromagnetic Spinor Bose-Einstein Condensate. Master's thesis, Universität Heidelberg, 2016.
- [20] Fam Le Kien, Philipp Schneeweiss, and Arno Rauschenbeutel. Dynamical polarizability of atoms in arbitrary light fields: general theory and application to cesium. *The European Physical Journal D*, 67(5):92, May 2013.
- [21] Anika Frölian. Implementation of local addressability in a bose-einstein condensate. Master's thesis, Universität Heidelberg, 2017.
- [22] J. M. Higbie, L. E. Sadler, S. Inouye, A. P. Chikkatur, S. R. Leslie, K. L. Moore, V. Savalli, and D. M. Stamper-Kurn. Direct nondestructive imaging of magnetization in a spin-1 bose-einstein gas. *Phys. Rev. Lett.*, 95:050401, Jul 2005.

Danksagung

An erster Stelle gebührt mein Dank Markus Oberthaler, der mir durch diese Arbeit meinen ersten experimentellen Kontakt zu diesem faszinierenden Themengebiet ermöglicht hat. Weiterhin erzeugt sein vertrauensvoller Umgang und die tiefgreifenden Diskussionen ein angenehmes Arbeitsklima, welches stets zu neuen Einsichten motiviert.

Dem gesamten BEC-Team möchte ich an dieser Stelle ebenfalls meine tiefste Dankbarkeit ausdrücken. Durch gegenseitigen Einsatz und ein freundschaftliches Miteinander lassen sich auch frustrierende Durststrecken gut überwinden. Max und Philipp möchte ich außerordentlich für das Beantworten meiner zahlreichen Fragen, die wiederholten Diskussionen und unzählige experimentelle Tricks danken. Vielen Dank auch für die Motivation in schwierigen Momenten und die zahlreichen Hilfestellungen in verschiedensten Situationen! Mein großer Dank gilt auch Helmut, der mir durch vielfältige Erklärungen und umfassende praktische Expertise nicht nur wertvolle Einblicke in die Physik, sondern auch Elektronik und Technik ermöglicht. Vielen Dank für die unschätzbaren Tipps, Anregungen und Motivationen (auch noch einmal Danke für den Verstärker). Anika möchte ich herzlich für die spannende Zeit mit den AODs während meinen ersten Tagen im Labor danken. Vielen Dank an Rodrigo und Alexis für den engen Austausch und immer wieder interessante Diskussionen zur Dynamik in unserem Kondensat und diversen experimentellen Techniken. Danke Daniel, für die physikalischen Hilfestellungen und erheiternden Ablenkungen. Auch Martin gebührt meine Dankbarkeit für die vielen Erklärungen und Gespräche, welche mir wiederholt hilfreiche Einblicke in die Theorie ermöglicht haben. Nicht zuletzt seinen hier natürlich auch unsere überaus entspannenden gemeinsamen (Labor)-abende erwähnt, auf welche ich mich stets wieder freue.

Darüber hinaus will ich mich bei der gesamten Matterwave-Gruppe bedanken, welche nicht nur den physikalischen, sondern auch gesellschaftlichen Austausch aktiv lebt. Insbesondere die zahlreichen Hilfestellungen und der Diskurs ständig neuer und spannender Probleme aus einem breiten Feld von unterschiedlichen Themen über die gesamte Gruppe hinweg ist ein überaus gewinnbringender Bestandteil dieser Gemeinschaft. Ebenso positiv sind natürlich auch unsere gemeinsamen Treffen zum Mittag- und Abendessen, sowie die zahlreichen weiteren Aktivitäten hervorzuheben. In diesem Sinne, Danke an BECK, AEgIS, ATTA, NaLi und alle Theoretiker. Ich bin glücklich ein Teil dieses vielfältigen und großartigen Teams sein zu dürfen!

Ein weiterer herzlicher Dank gebührt meinen Eltern für ihren bedingungslose und andauernde Unterstützung in allen Lebenslagen.

Erklärung:

Ich versichere, dass ich diese Arbeit selbstständig verfasst habe und keine anderen als die angegebenen Quellen und Hilfsmittel benutzt habe.

Heidelberg, den 20.04.2018

.....